Computers & Fluids 91 (2014) 144–163

Contents lists available at ScienceDirect

Computers & Fluids

journal homepage: www.elsevier.com/locate/compfluid

Immersed boundary method for pulsatile transitional flow in realistic cerebral aneurysms ☆

Julia Mikhal [a,*], Bernard J. Geurts [a,b]

[a] Multiscale Modeling and Simulation, Department of Applied Mathematics, University of Twente, P.O. Box 217, 7500 AE Enschede, The Netherlands
[b] Anisotropic Turbulence, Department of Applied Physics, Eindhoven University of Technology, P.O. Box 513, 5600 MB Eindhoven, The Netherlands

ARTICLE INFO

Article history:
Received 20 June 2013
Received in revised form 17 November 2013
Accepted 2 December 2013
Available online 17 December 2013

Keywords:
Cerebral aneurysm
Pulsatile flow
Immersed boundary method
Transition
Computational modeling of cerebrovascular flow
Patient-specific data

ABSTRACT

We adopt a volume penalizing immersed boundary method for the simulation of pulsatile blood flow inside cerebral aneurysms. We show that the flow undergoes a transition from an orderly state at low physiological Reynolds numbers, in which the pulsatile forcing is closely followed in time, to a complex response with strongly increased high-frequency components at higher physiological Reynolds numbers, i.e., at higher flow rates and larger aneurysm sizes. The flow is computed by solving the Navier–Stokes equations for incompressible flow. Geometric complexity of aneurysms in the cerebrovascular system is captured by defining the fluid and solid domains using a so-called binary 'masking function', which is a key element in the immersed boundary method. The pulsatile variation of the flow rate is represented in terms of measured cross-sectionally averaged velocities in the vicinity of the aneurysm, obtained by noninvasive Transcranial Doppler sonography. Transition of the flow is found to arise in qualitatively the same way at all locations near the aneurysm bulge, quite independent of the solution component that is monitored. The numerical reliability of the predicted transition is quantified on the basis of practical upper and lower bounding solutions, expressing the sensitivity of the flow to uncertainties in the aneurysm geometry. We compute the spectrum of the response of the flow at various locations and flow conditions and quantify the transition in local pressure and velocity. The significant increase of small-scale, high-frequency structures at higher Reynolds numbers may have potential for clinical screening application in the future.

1. Introduction

Prediction of blood flow inside cerebral aneurysms is a field of intensive research, aimed at supporting medical decisions about possible treatment strategies [18,23]. The cerebrovascular system has a complex geometrical structure, which varies from one person to another [46]. Also the properties of the blood flow, such as flow rate, viscosity and the actual profile of the heart beat are patient-specific characteristics. These days medical imaging techniques such as 3D rotational angiography (3DRA) can be used for diagnostic purposes, to visualize the vascular structure of the human brain [43]. Likewise, the actual pulsatile volumetric flow rate can be measured in a non-invasive way using a Transcranial Doppler (TCD) Sonography technique, which allows to record the time-dependent cross-sectionally averaged velocity in a chosen cerebral artery near the aneurysm [37]. Combining these two sources of medical data – geometry and pulsatile wave – we can develop new computational fluid dynamics (CFD) methods to actually compute the detailed blood flow on a patient-specific basis and ultimately try to understand hemodynamic aspects of slow aneurysm growth and developing risk of rupture.

In this paper we present a computational model for the flow of blood which allows to simulate pulsatile flow. The model is based on a finite volume discretization of the Navier–Stokes equations, while the geometry is represented using an immersed boundary (IB) method. The pulsatile wave is imposed as a forcing to the flow rate in the computational domain. By changing the flow conditions within the physiologically realistic range, we observe a striking transition from relatively smooth and regular flow to highly complex erratic time-dependence. To illustrate this transition we simulate the blood flow under different Reynolds numbers. This yields dynamic behavior ranging from smooth flow that closely follows the pulsatile forcing profile at the lower Reynolds range to very complex flow at the higher Reynolds range that appears much less connected to the regular forcing and displays significantly more contributions from high frequencies. These might be an indication of an increased size of the aneurysm, or more vigorous flow. The strong transition that we observed was also

☆ This manuscript is submitted as an original article.

* Corresponding author. Address: Multiscale Modeling and Simulation, Faculty EEMCS, University of Twente, P.O. Box 217, 7500 AE Enschede, The Netherlands. Tel.: +31 53 489 3418, fax: +31 53 489 3488.
E-mail address: j.mikhal@ewi.utwente.nl (J. Mikhal).

0045-7930/$ - see front matter © 2013 Elsevier Ltd. All rights reserved.
http://dx.doi.org/10.1016/j.compfluid.2013.12.009

reported earlier in clinical settings [9,20], and may be of medical use in rapid first monitoring of patients. In this paper we will illustrate this transition process for one particular patient's aneurysm geometry. We also considered other typical cerebral aneurysm geometries for which a similar transition was found in the same Reynolds range.

The capability to simulate the main flow structures in a realistic aneurysm can also be applied to understand the effect of coiling of patients from a fluid-mechanical point of view. The aim of the coiling procedure is to change the pattern of the flow such that the stream of blood is (largely) prevented from entering the weakened area of the vessel. This is approached by filling the bulge of the aneurysm with a slender coil. More recently, this goal is also pursued using flow diverting stents [41]. Since coiling is an operation with some risk to the patient one would like to predict the minimal amount of coiling that would be needed to achieve the required qualitative change in the flow. We illustrate the changes in the flow pattern inside and near a realistic aneurysm bulge that arise when partially filling it with a coil and observe the disappearance of the separated vortical flow pattern with increasing fraction of coiled volume in the bulge.

Various studies involving computational modeling of cerebral aneurysms were presented in literature in the past decade [4,7,10,33,40]. There has been a growing interest in the coupling of numerical and statistical techniques to investigate cerebral aneurysms [4,5,13,34]. The development process of numerical methods for simulation of blood flow typically goes through a number of stages: investigation of model geometries, computation of model flow, inclusion of realistic geometries and simulation of full-scale realistic flow yielding patient-specific results. For simulating pulsatile flow one may start with validation based on periodic sinusoidal forcing of the flow rate or other simplified forcing profiles [15,42,44]. Once the temporal accuracy is assessed one may continue by imposing recorded volumetric flow rates per heart beat as inflow to the system [1,22]. The development of the IB method used in this paper for capturing flow in cerebral aneurysms also went through these stages [24,25,28,26]. In this paper we complete the development of a first sequence of modeling steps by incorporating realistic pulsatile flow in realistic cerebral aneurysm geometries. We investigate the dynamic response of the flow in the aneurysm neighborhood and aneurysm bulge, for a range of physiologically relevant conditions.

We simulate pulsatile flow for different flow regimes, which are specified by the Reynolds number. A typical Reynolds number based on the radius of a cerebral vessel in the Circle of Willis is around 250. Due to uncertainty in various parameters a physiologically relevant range Re = 100–400 can be defended [9,10,38]. Under steady boundary conditions, this range corresponds to smooth laminar flow [11]. However, under unsteady boundary conditions, at the higher end of the Reynolds range rapid variations of the solution in time, sometimes wrongly referred to as 'turbulent' effects [2,9], were observed. In such flow conditions, diseased vessels support flows with rapid fluctuations, which could be detected via non-invasive techniques. These so-called brain 'bruits' can be recorded and the spectrum of frequencies can give some characterization of the shape and size of the aneurysm, as well as of the dominant flow regime [19,20].

Simulating flow on the basis of an IB method allows to go from medical imagery to quantitative flow predictions. We compute pulsatile flow inside and near a cerebral aneurysm and show that already at physiologically relevant flow conditions complex dynamics occurs. Quantitatively the level of shear stresses that is found numerically corresponds to values known from medical practice, thereby providing additional validation for the computations. With changing flow condition through increasing Reynolds number we observe transition in all sorts of quantities such as velocity components, pressure and shear stresses at various locations inside the vessels and aneurysm bulge. While analyzing the spectrum of the resulting numerical solution, the complex and more intense dynamics of higher Reynolds flows can be clearly observed.

The organization of this paper is as follows. In Section 2 we present the computational model for pulsatile blood flow simulations inside cerebral vessels. We first introduce the numerical method and aneurysm geometry, obtained from medical data. Then, we illustrate the reference steady state solution computed in the selected geometry and in partially filled cerebral aneurysms obtained from virtual coiling. Next in Section 3 we describe the pulsatile forcing of the blood flow, measured in an artery of the Circle of Willis and discuss the realistic range of parameters characterizing cerebral blood flow. Subsequently, we compute the solution in the selected geometry under reference pulsatile flow conditions at $Re = 250$. In Section 4 we present results obtained at different flow regimes and illustrate the transition arising in the flow at various locations inside the vessel and the aneurysm. We discuss the robustness of the transition phenomenon subject to uncertainties in the geometry definition by computing practical upper and lower bounding solutions. Finally, we perform a Fourier analysis to quantify frequencies of the pulsatile flow computed in the different flow regimes. Concluding remarks are in Section 5.

2. Computational model of cerebral blood flow

In this section we present the computational model for simulating blood flow inside cerebral vessels and aneurysms. We first discuss the Navier–Stokes equations and introduce the IB method, which allows to capture flow in complex domains. We illustrate this for a realistic aneurysm geometry, reconstructed from medical data in Section 2.1. Later, in Section 2.2, we simulate the reference flow in partially filled cerebral aneurysms, expressing the qualitative changes in the flow patterns due to 'virtual' coiling.

2.1. Immersed boundary method and aneurysm geometry

Modeling of blood flow in a human body can be performed in different ways depending on the particular flow regime that is relevant to the medical problem. A broad overview of models of the cardiovascular system is presented in [36]. Blood flow can be considered on the macroscopic scale – the level of fluid patterns, as well as on much smaller microscopic scales – blood cells and their bio-chemical transport processes. A first decision that is required when developing a model is whether or not to approximate blood as a Newtonian or a non-Newtonian fluid [3,5,10,12,16]. For cerebral flows taking into account physiological flow conditions and sizes of arteries the non-Newtonian corrections were found to be quite small [12,16,35]. Flow patterns were found to be qualitatively the same, while local values of velocities and pressures were found to differ by less than 20%.

In our numerical model blood is treated as an incompressible Newtonian fluid, for which the Navier–Stokes equations in 3D provide the conservation of mass and momentum. The total physical domain Ω, consists of a fluid part Ω_f that corresponds to the vessels containing the blood, and a solid part Ω_s that contains the soft tissue material. The no-slip condition is applied at the interface between fluid and solid parts in Ω. In non-dimensional form the governing equations are given by:

$$\frac{\partial \mathbf{u}}{\partial t} + \mathbf{u}\cdot\nabla\mathbf{u} = -\nabla P + \frac{1}{Re}\nabla^2\mathbf{u} + \mathbf{f} \tag{1}$$

$$\nabla\cdot\mathbf{u} = 0 \tag{2}$$

where $\mathbf{u}$ is the velocity of the fluid, P is the pressure, Re is the Reynolds number: $Re = U_r L_r/\nu_r$, based on the reference velocity

U_r, reference length scale L_r and reference kinematic viscosity ν_r . Finally, $\mathbf{f}$ is a forcing term that is used to represent the impenetrability of complex shaped solid vessel walls. For the forcing term we select a direct volume penalization [30] in which

$$\mathbf{f} = -\frac{1}{\varepsilon} H\mathbf{u} \tag{3}$$

where $\varepsilon \ll 1$ is a forcing parameter, taken in our simulation equal to $\varepsilon = 10^{-10}$. In Section 3.3 we will show more details regarding the choice of the penalty parameter ε. The forcing is defined in terms of the masking function H, given by $H(\mathbf{x}) = 0$ if $\mathbf{x} \in \Omega_f$ and $H(\mathbf{x}) = 1$ if $\mathbf{x} \in \Omega_s$. In this form the forcing term $\mathbf{f}$ allows to approximate the no-slip condition at the complex interface boundaries.

We solve the Navier–Stokes equations by employing symmetry-preserving finite volume discretization, closely following [45]. The key aspect of this discretization is strict energy conservation as basic property of both the continuous and the discrete equations. Specifically, we focus on the kinetic energy, given by

$$E = \frac{1}{2}\int_\Omega dV \mathbf{u}\cdot\mathbf{u} \equiv \frac{1}{2}(\mathbf{u},\mathbf{u}) \tag{4}$$

where $\mathbf{u}\cdot\mathbf{u}$ is the vector inner product and $(\mathbf{u},\mathbf{u})$ is the corresponding 'function inner product' in terms of the velocity field $\mathbf{u}$. Note, that in Eq. (4) we effectively integrate only over Ω_f as $\mathbf{u} = \mathbf{0}$ in Ω_s. The evolution of the kinetic energy dE/dt follows from multiplying the momentum Eq. (1) by $\mathbf{u}$ and integrating over the flow domain by parts. We then may derive the contribution of each of the fluxes in (1), establish that the convective and pressure terms do not contribute to the evolution of E, and find

$$\frac{dE}{dt} = -\frac{1}{Re}\int_\Omega dV(\nabla\mathbf{u} : \nabla\mathbf{u}) \leqslant 0 \tag{5}$$

where $\nabla\mathbf{u} : \nabla\mathbf{u} = \partial_i u_j \partial_i u_j$ in which we sum over repeated indices. Hence, the kinetic energy decreases in time because of viscous fluxes only. This basic property of the Navier–Stokes equations is also basic for the developed discretization, as we endeavour to maintain this property also on the discrete level.

In a discrete setting the Navier–Stokes equations (without the forcing term $\mathbf{f}$) in matrix–vector notation may be written as

$$\mathbf{\Lambda}\frac{d\mathbf{u}_h}{dt} = -\mathbf{C}\mathbf{u}_h - \mathbf{D}\mathbf{u}_h + \mathbf{M}^T\mathbf{P}_h \tag{6}$$

$$\mathbf{M}\mathbf{u}_h = \mathbf{0} \tag{7}$$

where $\mathbf{u}_h$ is the vector containing the discrete velocity solutions $u_i^{(h)}$, $\mathbf{P}_h$ is the discrete pressure, $\mathbf{\Lambda}$ is a diagonal matrix with the volumes of the grid cells on its diagonal, $\mathbf{C}$ and $\mathbf{D}$ are the coefficient matrices corresponding to the discretization of the convective $((\mathbf{u}\cdot\nabla)\mathbf{u})$ and diffusive $(-\Delta\mathbf{u}/Re)$ operators, respectively. The discretization of the pressure gradient is given by $-\mathbf{M}^T$, while the coefficient matrix $\mathbf{M}$ itself represents the discretization of the divergence operator [45]. The discrete approximation for the kinetic energy can be given as

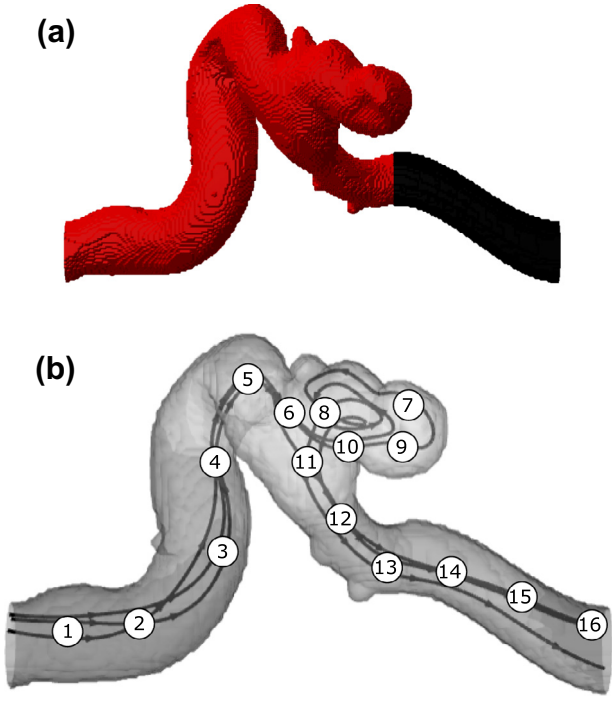

Fig. 1. 3D masking function for aneurysm geometry (a) and typical streamlines with indication of the monitoring points of interest (b). The cut part of the geometry is plotted in red, while the connecting vessel is shown in black (a). Streamlines in (b) illustrate simulations of steady flow at $Re = 250$.

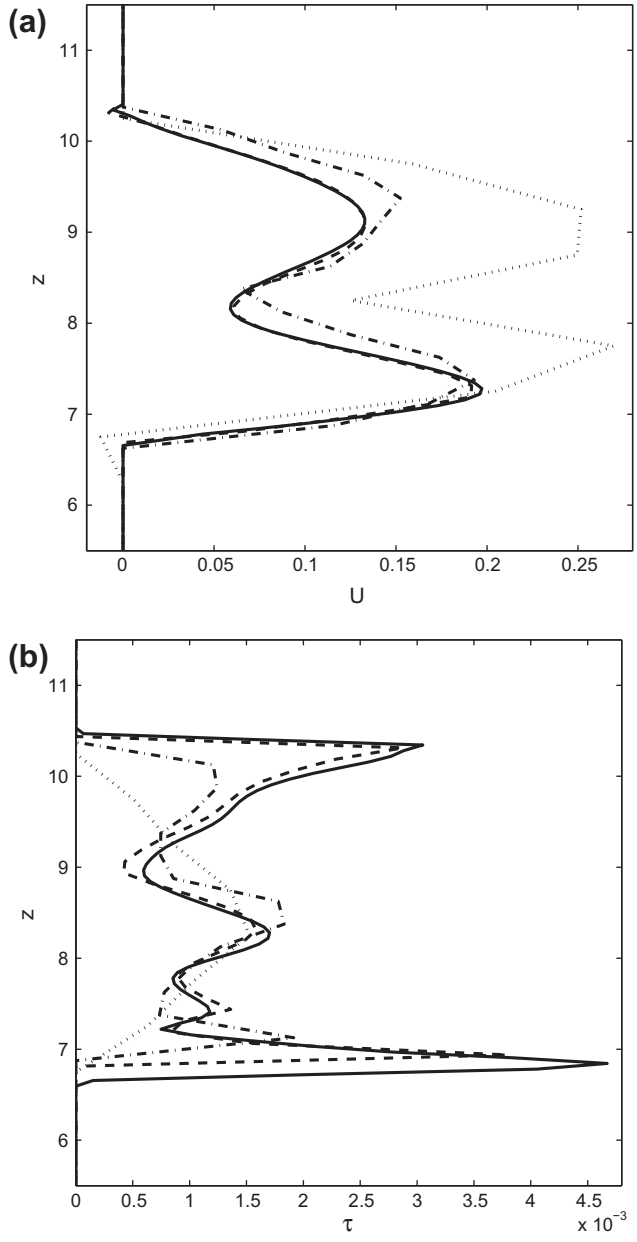

Fig. 2. Velocity profiles (a) and shear stresses (b) computed at several grid resolutions ($32\times16\times32$ – dot, $64\times32\times64$ – dash-dot, $128\times64\times128$ – dot, $256\times128\times256$ – solid) in the cross-section close to the aneurysm bulge.

$$E_h = \mathbf{u}_h^T \Lambda \mathbf{u}_h \tag{8}$$

The evolution of the energy in the discrete model may be computed as

$$\frac{dE_h}{dt} = -\mathbf{u}_h^T(\mathbf{C}+\mathbf{C}^T)\mathbf{u}_h - \mathbf{u}_h^T(\mathbf{D}+\mathbf{D}^T)\mathbf{u}_h + \mathbf{u}_h^T(\mathbf{M}^T\mathbf{P}_h) + (\mathbf{M}^T\mathbf{P}_h)^T\mathbf{u}_h \tag{9}$$

For the discrete solution we also require the convective conservation of energy, which implies skew-symmetry of the matrix $\mathbf{C}$ of the convective operator: $\mathbf{C}+\mathbf{C}^T = \mathbf{0}$. The two terms related to the numerical pressure gradient can be rewritten as

$$\mathbf{u}_h^T(\mathbf{M}^T\mathbf{P}_h) + (\mathbf{M}^T\mathbf{P}_h)^T\mathbf{u}_h = (\mathbf{M}\mathbf{u}_h)^T\mathbf{P}_h + \mathbf{P}_h\mathbf{M}\mathbf{u}_h = \mathbf{0} \tag{10}$$

where the numerical divergence of the numerical velocity satisfies Eq. (7). Thus, pressure terms also do not contribute to the evolution of the kinetic energy in the discrete formulation. By comparison with the expression for the energy evolution Eq. (5), the second term on the right-hand side of (9) should provide a strict decrease of the energy:

$$\frac{dE_h}{dt} = -\mathbf{u}_h^T(\mathbf{D}+\mathbf{D}^T)\mathbf{u}_h \leqslant 0 \tag{11}$$

This implies that the coefficient matrix $\mathbf{D}$ of the diffusion operator is a positive-definite matrix.

Thus, discretely we obtain the same properties for the energy decay as in the continuous case if (i) the convective terms are discretised with a skew-symmetric method, (ii) the numerical divergence matrix is the transpose of the numerical gradient and (iii) the numerical diffusive flux is represented by a positive definite matrix. Here we adopt such a method and in particular follow the approach presented in [45].

Since kinetic energy is preserved under the skew-symmetric discretization a stable solution may be obtained on any grid. We use central differencing of second order accuracy, which maintains explicitly the skew-symmetry in the discrete equations. The contributions of the convective, viscous and pressure-gradient fluxes are integrated in time using a generalization of the explicit second order accurate Adams–Bashforth method. Care is taken of accurately representing the skew-symmetry also in the time-integration. Full incorporation would require an implicit time-stepping, which, however, is computationally too demanding. Instead, time-integration starts from a modification of the leapfrog method with linear inter/extrapolations of the required 'off-step' velocities and an implicit treatment of the incompressibility constraint. Optimization for largest stability region of the resulting scheme yields a particular so-called 'one-leg' time-integration method, with a mathematical structure that is akin to the well-known Adams–Bashforth scheme. More details can be found in [45]. For the forcing term such explicit time-stepping would result in extremely small time-steps in view of numerical stability. Therefore, the linear forcing term is integrated in time using the implicit Euler scheme.

Complex aneurysm geometries are represented by the masking function H, which is a key element of our IB method as it defines fluid and solid parts of the computational domain. In fact, for those regions, where $H = 0$ the Navier–Stokes system is solved. In the regions where $H = 1$ the forcing term provides control over the velocity in the tissue basically representing no-flow in the tissue. Validation of our numerical model for Poiseuille type of flow in cylindrical pipe, curved vessels and model aneurysm geometry can be found in [28].

We adopt periodic boundary conditions for the velocity components on the computational domain Ω. The pressure P is

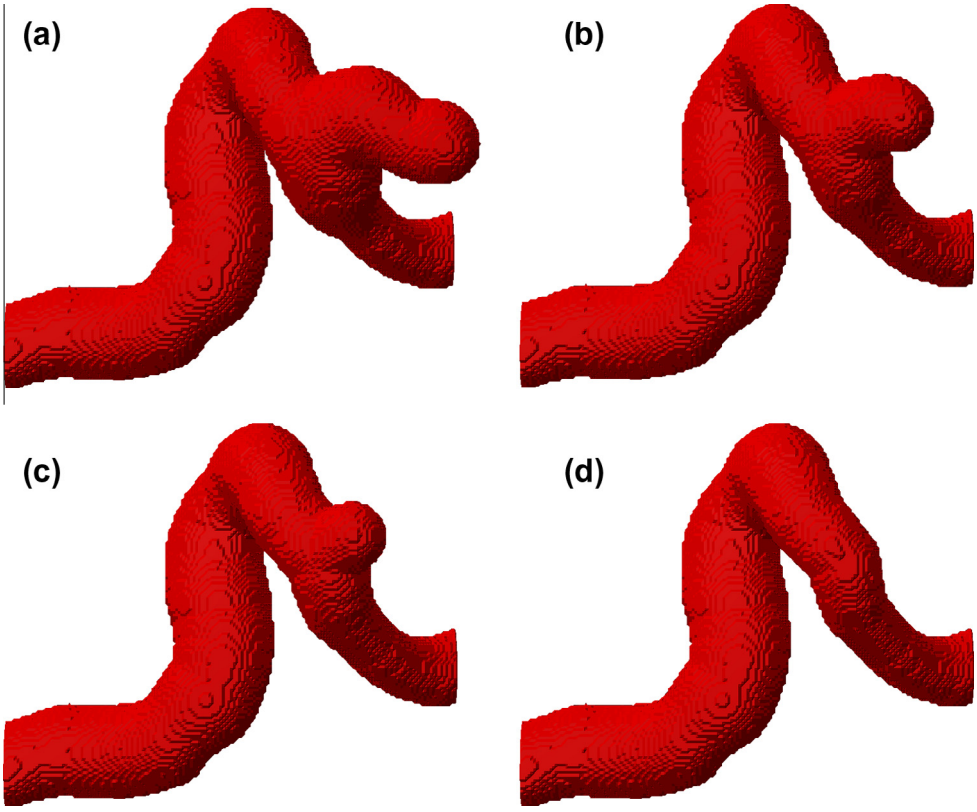

Fig. 3. Masking functions for partially filled aneurysms. Starting from the reference geometry (a) we can virtually fill the aneurysm with a coil and obtain the reduced shapes in (b) and (c). The fully coiled aneurysm is shown in (d).

decomposed as $P = p + a(t)x$, where p is a strictly periodic component and $a(t)$ is continuous time-dependent function adapted at every time-step, such that the prescribed flow rate is maintained. In this way periodic conditions are established on the total computational domain, which implies proper connection of the 'corresponding' fluid parts of the domain effectively linking the outflow to the inflow of the geometry through the introduction of a smooth segment of vessel that takes care of the flow feedback, much in the same vein as the fringe region introduced in [39]. While generating the masking function, additional operations must be performed in order to satisfy periodicity. Thus, we start with the medical images obtained from the 3DRA procedure recording the local vessel structure and the possible brain aneurysm. We perform standard segmentation and simplification processes in order to separate the main relevant vessel segment. In more details these procedures as well as choice of corresponding parameters are discussed in [29]. Afterwards, we perform additional operations as 'cutting' away parts of the vasculature far away from the aneurysm bulge and 'connecting' ends of the vessel by a smooth connector assuring periodicity of the fluid domain. In [29] we analyzed sensitivity of the flow predictions to the differently cut geometries or adding not only smooth connectors but also linear. It was shown that the flow inside the aneurysm bulge is not affected much, if cuts are made far away (2–3 radii of the vessel opening) from the aneurysm bulge.

In this paper we work with a geometry, reconstructed from 3DRA data as shown in Fig. 1(a). The part of the original geometry that is retained in the computational model is plotted in red, while the smooth connector based on cubic spline interpolation is shown in black. The initial medical data of the 3DRA scan consists of 256^3 voxels, with voxel width 0.1213 mm. This leads to a total physical length of the domain of 3.10528 cm. For numerical simulations it is convenient to work in the non-dimensional setting, for which all values for length, velocity, time, etc. are scaled by reference parameters. The system after scaling remains a pure analogy of the physical system, and translations back and forward are always possible. In case of vessels and aneurysms, the radius of the vessel is a suitable reference length [10,38]. We extract $R = 1.94$ mm from the 3DRA data, which brings us to a domain of length $31.0528/1.94 \sim 16$ in the non-dimensional formulation. Moreover,

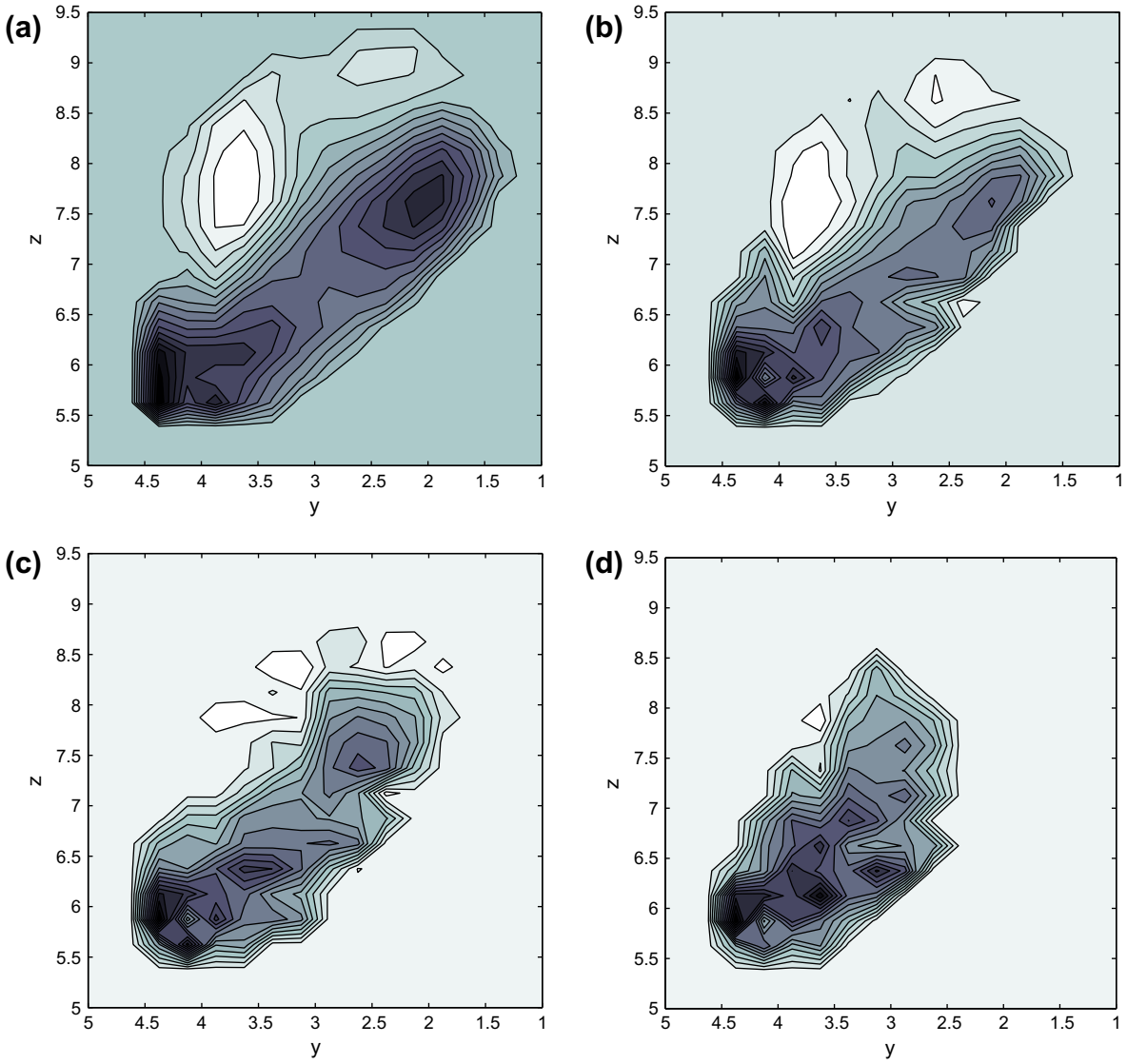

Fig. 4. Contour plot of the streamwise velocity in a *yz* cross-section in the middle of the geometry in partially filled aneurysms. Dark regions correspond to positive velocities, while the lightest (white) contours are related to regions of negative velocity; we adopt the same color-coding for all figures. The flow structures show a large vortex in the reference geometry of the aneurysm (a) and in the slightly coiled aneurysm (b) seen because both positive and negative velocities occur, while with increasing coiled volume the vortical pattern reduces considerably (c) and disappears in the fully coiled case (d) approximately restoring the original non-diseased geometry.

for the particular geometry we noticed that after segmentation and additional steps of cutting and connecting, the vessels filled only half of the volume in the y direction. This allows to remove the 3D tissue-cells in half of the domain as there is no flow in this part of the computational model. Thus, we arrive at a computational domain of length $L_x \times L_y \times L_z = 16 \times 8 \times 16$ and use grid resolution up to $n_x \times n_y \times n_z = 256 \times 128 \times 256$ to represent the geometry.

For simulations of steady flow in [27] we considered also coarsened grids of resolutions $128 \times 64 \times 128, 64 \times 32 \times 64$ and $32 \times 16 \times 32$. Later, in [29] we improved the computation of the shear stress by developing 'geometry-resolved' post-processing, in which knowledge of the highest resolved geometry was explicitly included in the computation of the stresses on one of the coarser grids. This allowed to obtain more accurate results near the fluid–solid boundaries as illustrated in Fig. 2. We may appreciate the level of convergence of the velocity from a characteristic profile taken near the aneurysm bulge (Fig. 2(a)). Similarly, Fig. 2(b) summarizes the convergence of the shear stress in case the geometry-resolved post-processing is incorporated (for further details see also [27,29]).

We analyzed the convergence of the solution and could conclude that starting from a resolution of $64 \times 32 \times 64$ reliable results could be obtained. Under these resolution conditions a cross-section through a vessel is typically covered by about 15–20 grid cells in each coordinate direction. For Poiseuille flow it was found that under these resolution conditions the L_2-norm of the error in the velocity is maximally about 10% – this level of accuracy is considered reasonable for our purposes – higher accuracy requires a larger computational effort. During coarsening of the grid, bounding geometries can be systematically generated. These can be used to obtain the range of variability of the solution due to uncertainty in the precise flow domain, thereby further quantifying the quality of the predicted flow. In this paper we will simulate pulsatile flow at a grid resolution $64 \times 32 \times 64$. Typical velocity streamlines following the main vessel and coming into the aneurysm bulge are shown in Fig. 1(b). We also display schematically the approximate locations of several points of interest at which we will analyze the flow in more detail and investigate the transition. These points were chosen quite uniformly throughout the aneurysm geometry to analyze the flow dynamics in the vessel before, after and inside the aneurysm bulge.

2.2. Flow in partially filled cerebral aneurysms

With the IB method it is possible to generate various modified geometries in a relatively fast way, starting from the reference geometry. This allows to investigate consequences for the flow structure due to changes in the local vessel shape. Next to flow predictions in the initially reconstructed vascular geometry we can also simulate flow in 'nearby' geometries representing aneurysms that are 'virtually filled' with a slender coil. Such simulations can help to understand how much coil is necessary to qualitatively change the flow structure in the affected region, aimed at reducing the flow into the aneurysm bulge to make the situation less risky. To illustrate the approach, we generated three virtual geometries which correspond to partially or fully filled aneurysms. In these geometries we compute the blood flow and observe changes in the vortical flow patterns when increasing the amount of coil in the bulge.

In Fig. 3 we illustrate four masking functions which show possible stages during a coiling procedure. We start with the reference geometry in Fig. 3(a) and 'coil' the aneurysm bulge in two steps (Fig. 3(b and c)). The fully filled aneurysm is shown in Fig. 3(d). Analyzing flow patterns we plot the velocity contours in the middle cross-section of the aneurysm. We observe qualitative differences in the flow patterns when comparing the reference case and the slightly coiled geometry (Fig. 4(a and b)) with the further coiled and the fully coiled aneurysm (Fig. 4(c and d)). These simulations show the disappearance of the large vortical structure seen in the first two geometries – the backward flow is almost completely removed provided the amount of coil is adequate, as seen in the last two geometries. These differences in flow pattern can be relevant for decisions about the (minimal) amount of coil needed to achieve the required flow deflection.

We will concentrate on the reference geometry alone and continue with the realistic pulsatile flow simulations.

3. Pulsatile flow simulations

In this section we focus on pulsatile flow under realistic conditions. In Section 3.1, we concentrate on physiological aspects of cerebral blood flow and specify the pulsatile forcing, extracted

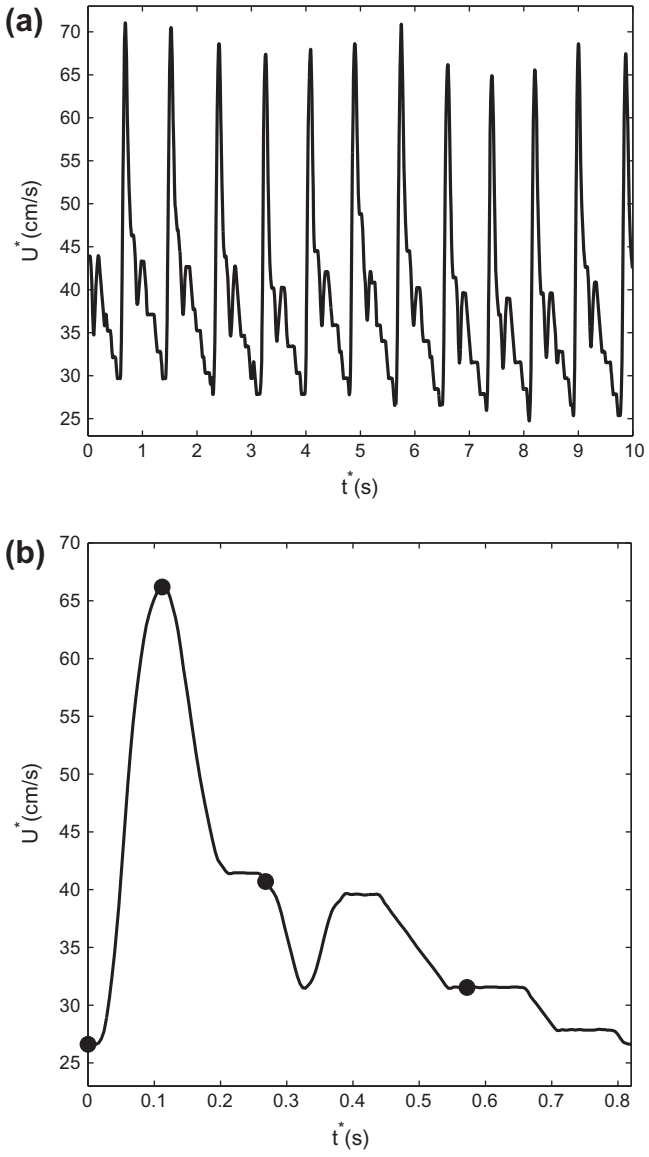

Fig. 5. Pulsatile velocity measured in the human brain using TCD sonography. Ten seconds velocity signal as measured in the MCA is presented in (a). The unit pulse (b) which was chosen from the original signal for computations contains also 4 points of interest during the cardiac cycle: $t_1 = 0.112$ s,$t_2 = 0.324$ s,$t_3 = 0.416$ s and $t_4 = 0.756$ s corresponding to peak systole, end systole, peak diastole and end diastole respectively.

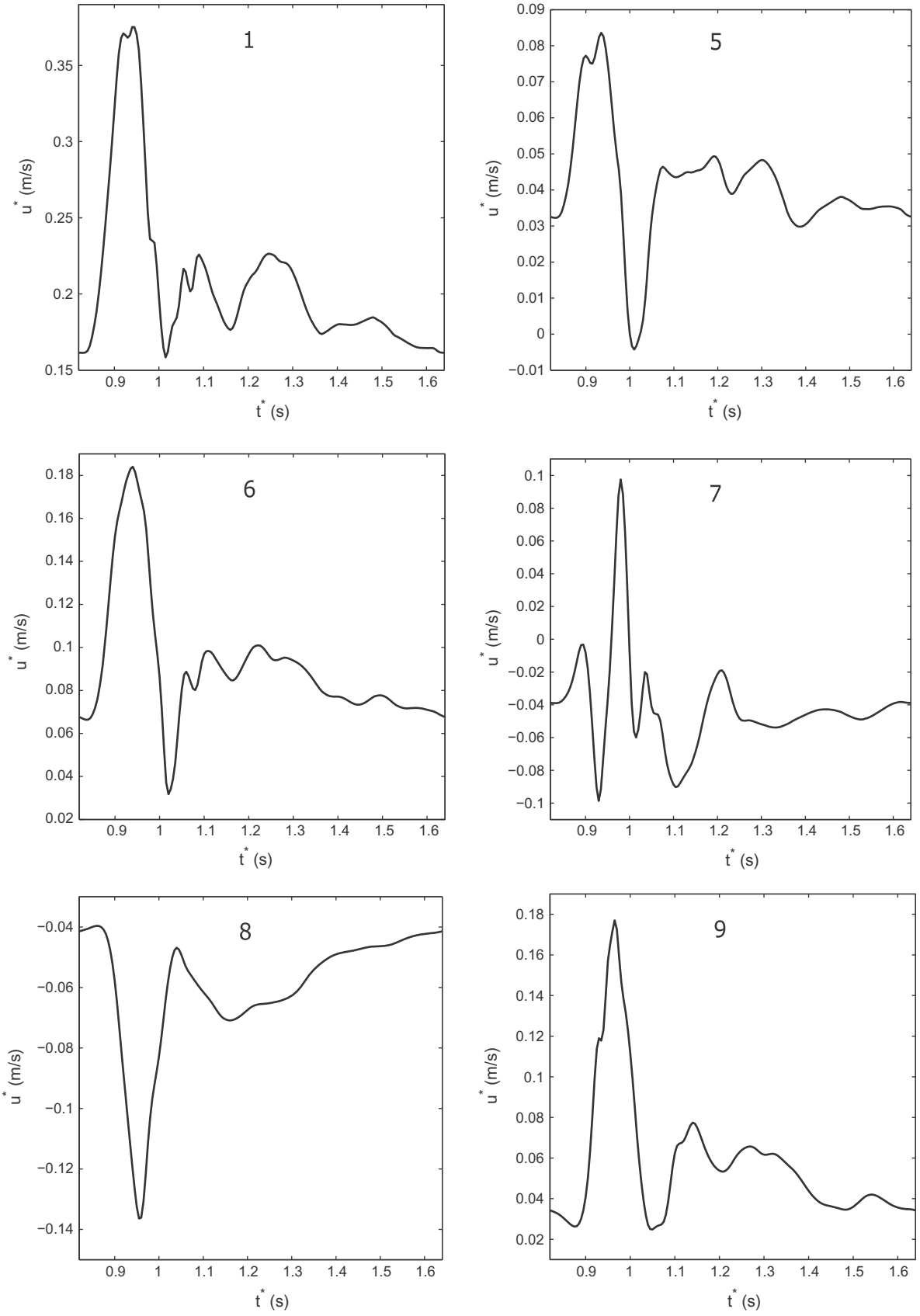

Fig. 6. Values of the x-wise velocity component during a heart beat at $Re = 250$ in 10 chosen locations along the aneurysm geometry. The number on top of every sub-figure corresponds to the label of the point, whose location is shown in Fig. 1(b).

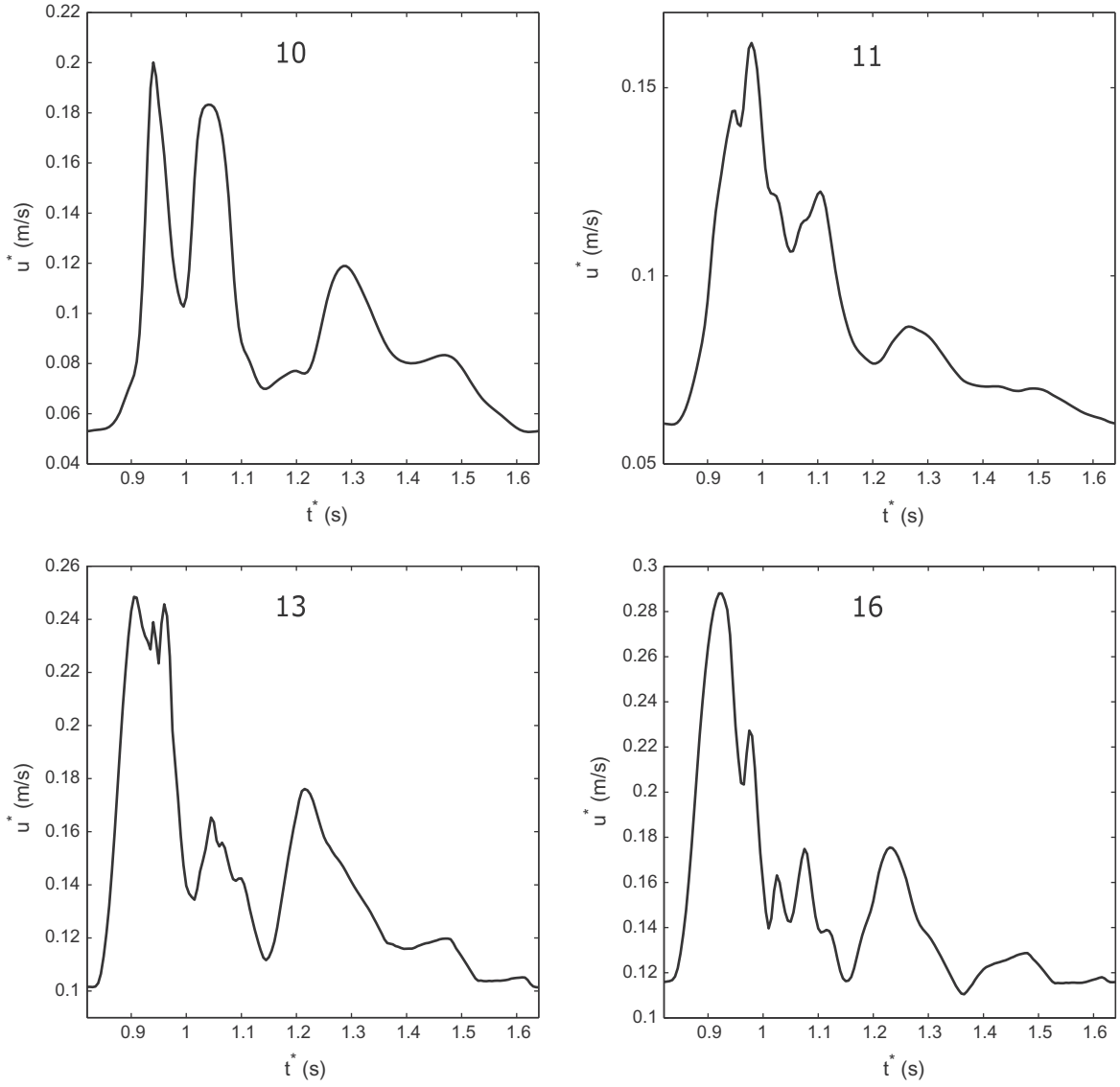

Fig. 6 (*continued*)

from TCD measurements. We also motivate the choice of flow parameters that characterize physiological conditions as used in the simulations. In Section 3.2 we present the computed velocities at different locations along the aneurysm geometry and at different stages during a heart-beat. In Section 3.3 we focus on the sensitivity of the predictions to the choice of the penalty parameter ε and the computational time-step Δt.

3.1. Flow conditions and pulsatile forcing

To complete the computational model we need to define flow conditions which are realistic for blood flow in cerebral vessels and aneurysms and specify the pulsatile cycle in the flow-rate which is used to force the flow. The only parameter which is responsible for specifying the flow regime in (1) is the Reynolds number $Re = U_r L_r / \nu_r$, where U_r, L_r and ν_r are reference velocity, length and viscosity correspondingly. The range of Reynolds numbers characteristic of blood flow in the Circle of Willis, corresponds to laminar flow. To quantify this, we estimate the Reynolds number for physiologically relevant conditions next.

The reference length L is chosen based on the average radius of the cerebral vessel in the scanned part of the Circle of Willis. For the given geometry $L_r = 1.94$ mm, which is consistent with [17] who found a value of 2.1 ± 0.4 mm. The reference kinematic viscosity of the blood can be found as the ratio between the dynamic viscosity of human blood and the mass density. These quantities differ from person to person. By choosing typical values for the mass density $\rho_r = 1060\ \mathrm{kg/m^3}$ and the dynamic viscosity $\mu_r = 3.2 \times 10^{-3}$ Pa s we arrive at a kinematic viscosity $\nu_r = 3.01 \times 10^{-6}\ \mathrm{m^2/s}$. To complete the estimate of the Reynolds number, the reference velocity is taken as the ratio between the average volumetric flow-rate of the blood going through the vessel and an approximation of the area of a cross-section through the vessel. The flow-rate for blood can be measured by means of 3D MR angiograms [14,31] in which values $Q = 245 \pm 65$ ml/min were found showing an uncertainty of about 25%. Based on the reference length L_r and an assumed circular cross section as approximation, the range for the reference velocity is $U = 0.345 \pm 0.09$ m/s. These values are in very close agreement with the range 0.34 ± 0.087 m/s as obtained by [37] on the basis of TCD measurements. Combining these reference scales we compute typical Reynolds numbers to be in the range of $175 \lesssim Re \lesssim 300$. As key reference Reynolds number we adopt $Re = 250$, which in terms of chosen reference length and kinematic velocity corresponds to a velocity scale $U_r = 0.388$ m/s. Later we will vary the Reynolds

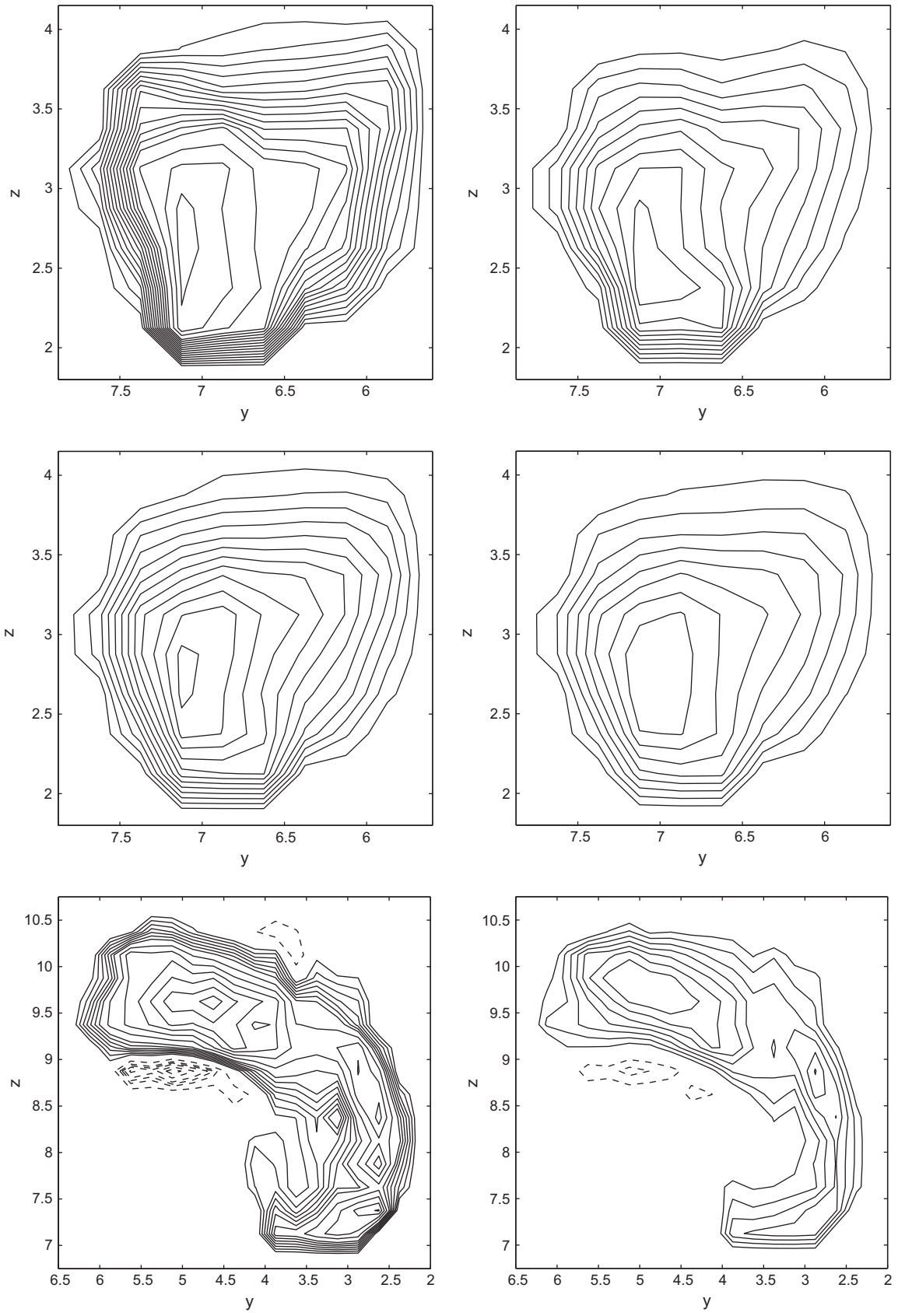

Fig. 7. Velocity patterns at different stages during the cardiac pulse in four cross-sections along the aneurysm geometry. The columns correspond to the stages of the cardiac cycle, related to peak systole, end systole, peak diastole and end diastole respectively. The rows correspond to the different cross sections along the aneurysm geometry. In the first and fourth rows we plot the cross sections at $x = L_x/8$ and $x = 7L_x/8$. The second and third rows correspond to the flow nearer the aneurysm bulge at $x = 0.4L_x$ and $x = 0.5L_x$. Simulations are at $Re = 250$.

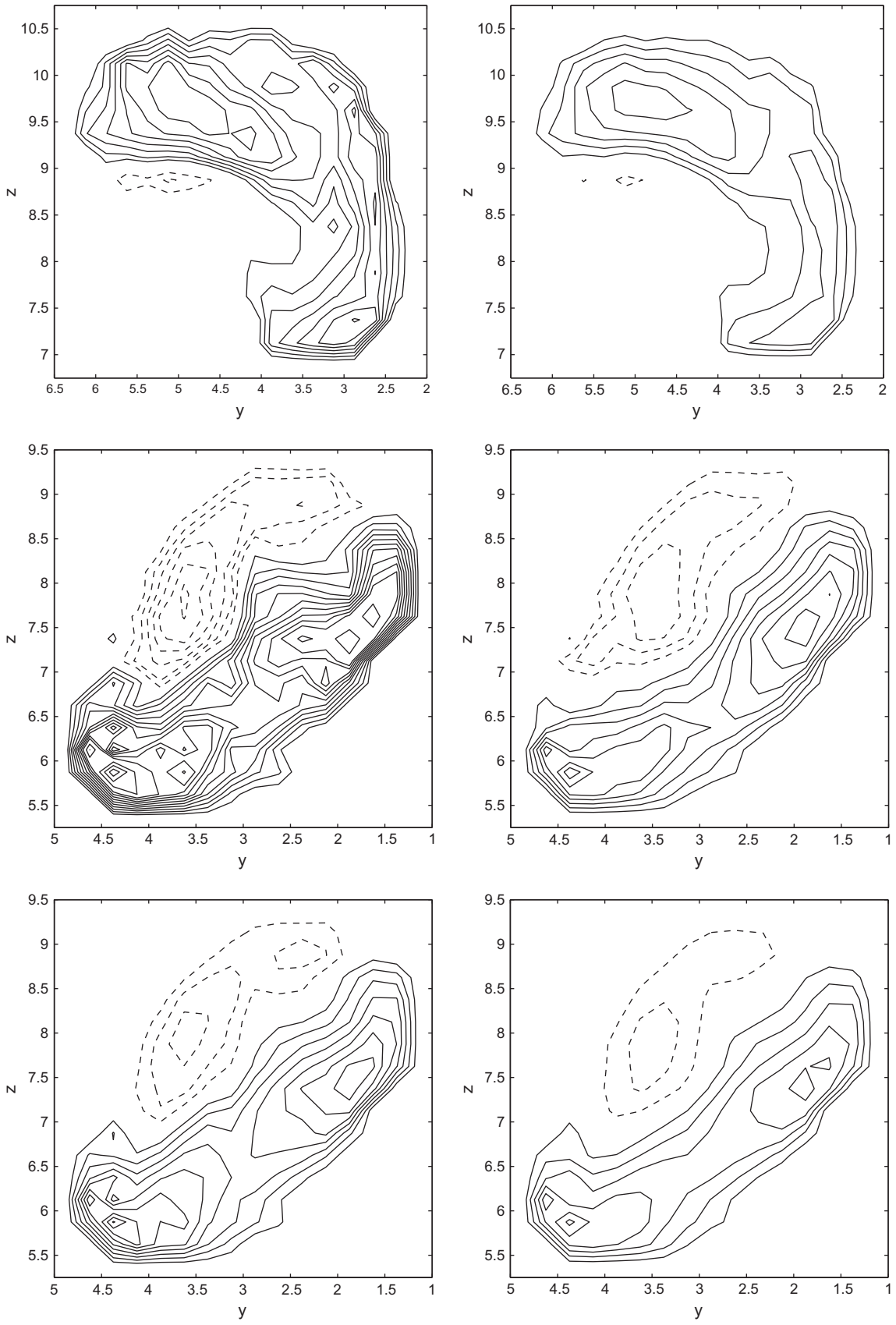

Fig. 7 (*continued*)

number to investigate the quantitative and qualitative sensitivity of the flow to this parameter. We also compute the flow at $Re = 200$ and $Re = 300$ as these reflect the differences in the blood viscosity, the sizes of the vessels and/or the velocity scales, which were found

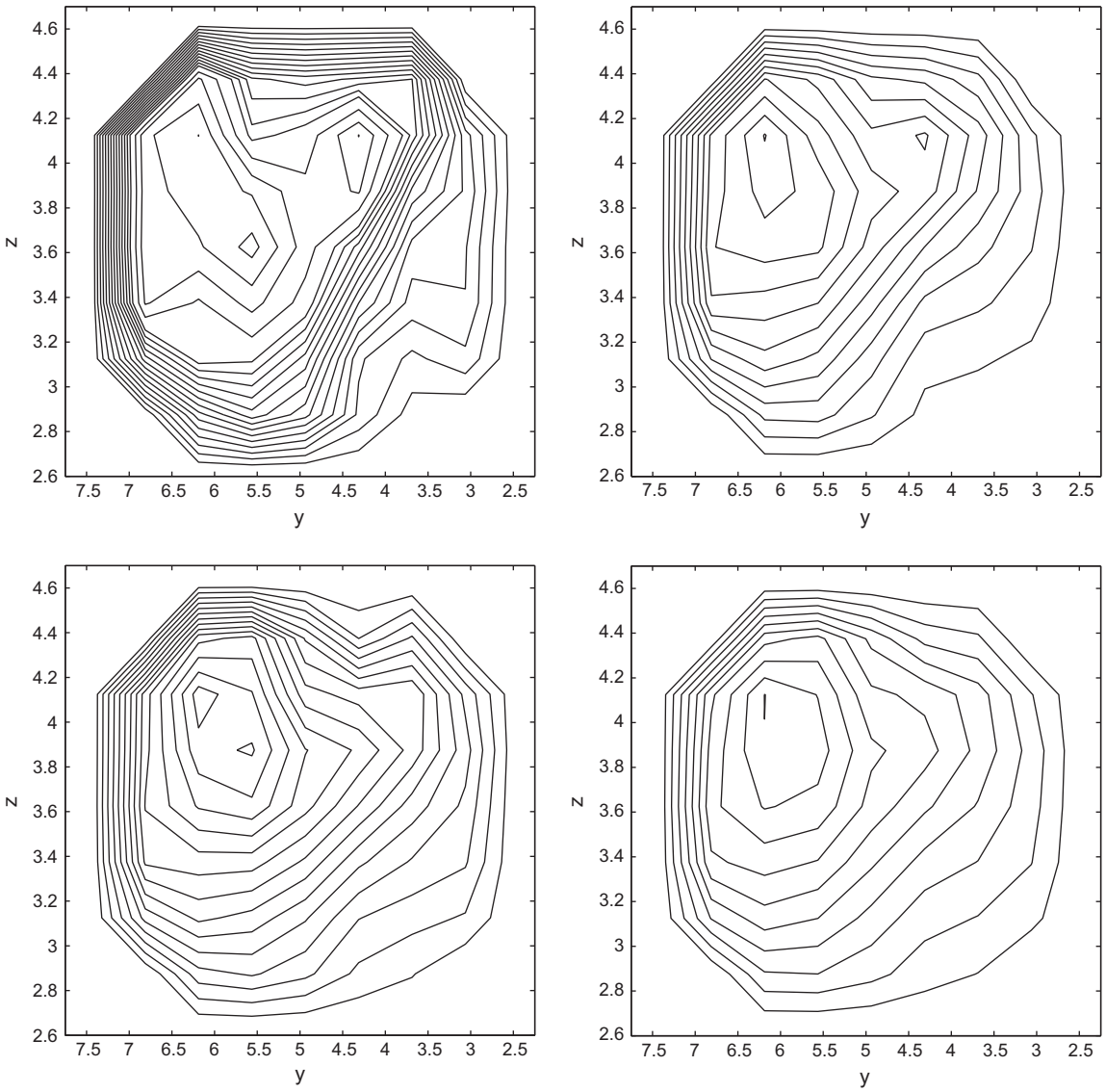

Fig. 7 (*continued*)

in literature. In case of diseased conditions we can expect an even wider range of Reynolds numbers, therefore we also compute the flow at $Re = 100$ and $Re = 400$. The same range of Reynolds numbers was suggested in [10,38], based on slightly different choices for diameter sizes and blood properties.

In order to compute pulsatile flow we need to impose a pulsatile cycle for the volumetric flow rate as an input for our numerical simulations. With the use of phase-contrast (MR) angiography [14,31] or TCD sonography [37] the time-dependent cross-sectionally averaged velocity of the blood flow in cerebral arteries can be measured. In the current study the velocity was recorded in the middle cerebral artery by [8] using TCD. In Fig. 5(a) we plotted a segment of 10 s of the pulsating velocity. The mean velocity value, obtained by integrating this signal, is found to be 38.66 cm/s, which is very close to the reference scale selected above.

The computed pulsatile flow is maintained by using the actually recorded velocity signal as forcing. We choose a typical pulse (Fig. 5(b)) and repeat it periodically. For our computations, we convert the recorded velocity pulse into a time-dependent volumetric flow rate. The selected pulse has a maximal velocity $U_{max} \approx 67.94$ cm/s, which corresponds to a peak flow rate of $Q_{max} \approx 8.033 \times 10^{-6}$ m^3/s, using the selected radius $R = L_r = 1.94$ mm and assuming a perfectly circular cross section. If we take the reference velocity $U_r = 0.388$ m/s corresponding to a Reynolds number $Re = 250$, we find similarly as reference flow rate $Q_r \approx 4.59 \times 10^{-6}$ m^3/s. For convenience, we split the forcing signal in the non-dimensional formulation into a normalized flow rate pattern Q_0 which varies between 0 and 1, and an amplitude Q_{max}/Q_r such that the forcing used in the simulations becomes $Q(t) = (Q_{max}/Q_r)Q_0(t) \approx 1.75Q_0(t)$. The physical duration of one pulse is $t = 0.82$ s. The reference time-scale can be computed as $t_r = R/U_r = 0.005$ s. Thus at $Re = 250$ one pulse requires 164 non-dimensional time units.

The procedure to define the pulsatile flow rate can be extended to also address other Reynolds numbers. We take as reference Reynolds number Re and fix the reference length-scale to L_r (since we consider the same geometry) and the kinematic viscosity to ν_r (since we still consider the flow of blood). If we wish to simulate at another Reynolds number Re' this implies that the reference velocity scale is changed according to $U_r' = (Re'/Re)U_r$. Correspondingly, the time-scale changes into $t_r' = (Re/Re')t_r$ and hence, the 'new' number of dimensionless time-steps to take in order to complete one cycle of 0.82 s of the pulsatile flow decreases with decreasing Reynolds number. Another consequence of changing

the Reynolds number at constant length-scale and kinematic viscosity is that $Q_r' = (Re'/Re)Q_r$, as well as $Q_{max}' = (Re'/Re)Q_{max}$. Hence, the dimensionless forcing does not alter with changing Reynolds number and remains at $Q(t) \approx 1.75Q_0(t)$. The factor 1.75 denotes the 'contrast' in the pulsatile flow rate, i.e., the ratio between the maximal and the average velocity during a cycle – this quantity varies from one person to another and even slightly per heartbeat. The change in Re corresponds to a change in U_r, which affects the scale for the shear stress which is $\rho_r(U_r)^2$. The final result will be presented in dimensional form and include a wall shear stress in *Pa* and time measured in *s*, which allows a direct comparison with literature.

3.2. Reference pulsatile flow

For the reference case we perform pulsatile simulations at $Re = 250$ and first illustrate velocity traces per cardiac cycle. In 16 points, illustrated in Fig. 1(b) we compute the velocity during one pulse and plot the results in characteristic points in Fig. 6. We observe complex patterns of the streamwise velocity at all locations. In some points the flow follows the pulsatile forcing profile, as we would expect for laminar flow in roughly cylindrical vessels, e.g., points 1, 13, 16. We also observe negative velocities, e.g., in point 5, 8, which are related to the recirculation of the flow.

In Fig. 7 we present 2D velocity contour plots at 4 different cross sections along the aneurysm geometry and at 4 different cardiac stages. Two cross sections (first and last rows) were chosen in the vessel parts close to the ends of the selected domain at $x = L_x/8$ and $x = 7L_x/8$. Two other cross sections (second and third rows) are taken closer to the aneurysm bulge, at $x = 0.4L_x$and $x = 0.5L_x$. The latter cross section was also analyzed for steady flow in Chapter 3. The first column corresponds to the peak systole stage, which displays a rather intense density of contour lines, indicating the wider range of values involved. The second column as well as the fourth column correspond to the ends of systole and diastole and display relatively more quiet flow patterns, while the third column is related to the peak diastole stage, which is less vigorous than peak systole as seen from the reduced number of contour lines compared to the first column. We plotted negative velocities as dashed lines, which are clearly present in the second and third rows, displaying the circulation of the blood flow near the aneurysm bulge. In the vessels far away from the aneurysm bulge (first and fourth rows) the flow behaves much as Poiseuille flow and negative velocities are not present. Similar results were obtained in [6] where the effect of flow rate during the cardiac cycle in different aneurysm geometries was investigated.

3.3. Sensitivity of the pulsatile response to the value of ε and Δt

A numerical analysis of the sensitivity of the numerical solution to changes in the penalty parameter ε was performed for the reference geometry. The results are presented in Fig. 8. The pulsatile response of the maximum shear stress shows a clear convergence with decreasing ε. A more quantitative analysis of the error reduction with decreasing ε is illustrated in Fig. 8(b), which illustrates first order convergence of the solution as function of the penalty parameter ε. We observe such first order convergence already as $\varepsilon \lesssim 10^{-3}$, and establish deviations less than 10^{-6} if $\varepsilon \lesssim 10^{-8}$, as already advised in [21]. Since computational costs are independent of the value of ε, in all simulations we choose $\varepsilon = 10^{-10}$ in order to accurately represent the non-penetrating solid interfaces of the domain.

We also analysed the sensitivity of the predicted pulsatile response to the chosen time-step in the computations. For this purposes we performed a set of test simulations in which the time-step was varied according to $\Delta t = 10^{-1}, 5\times10^{-2}, 10^{-2}, 5\times10^{-3}, 10^{-3}, 5\times10^{-4}, 10^{-4}, 5\times10^{-5}, 10^{-5}$ (in dimensionless units). Results for the maximum shear stress response of the flow computed during one pulse are presented in Fig. 9. Clear convergence is observed starting from the solution at $\Delta t = 10^{-3}$. The converge is presented more quantitatively by presenting the L_2-norm of the difference between the numerical solution computed at the smallest $\Delta t = 10^{-5}$ with all other numerical solutions computed at bigger time steps. First order convergence is observed with respect to Δt as shown in Fig. 9(b). Based on this analysis we chose $\Delta t = 10^{-4}$ as a suitable time step for the reference case. Simulations with this time-step for the given geometry take a few hours on 16 CPU's which makes it realistic for the application.

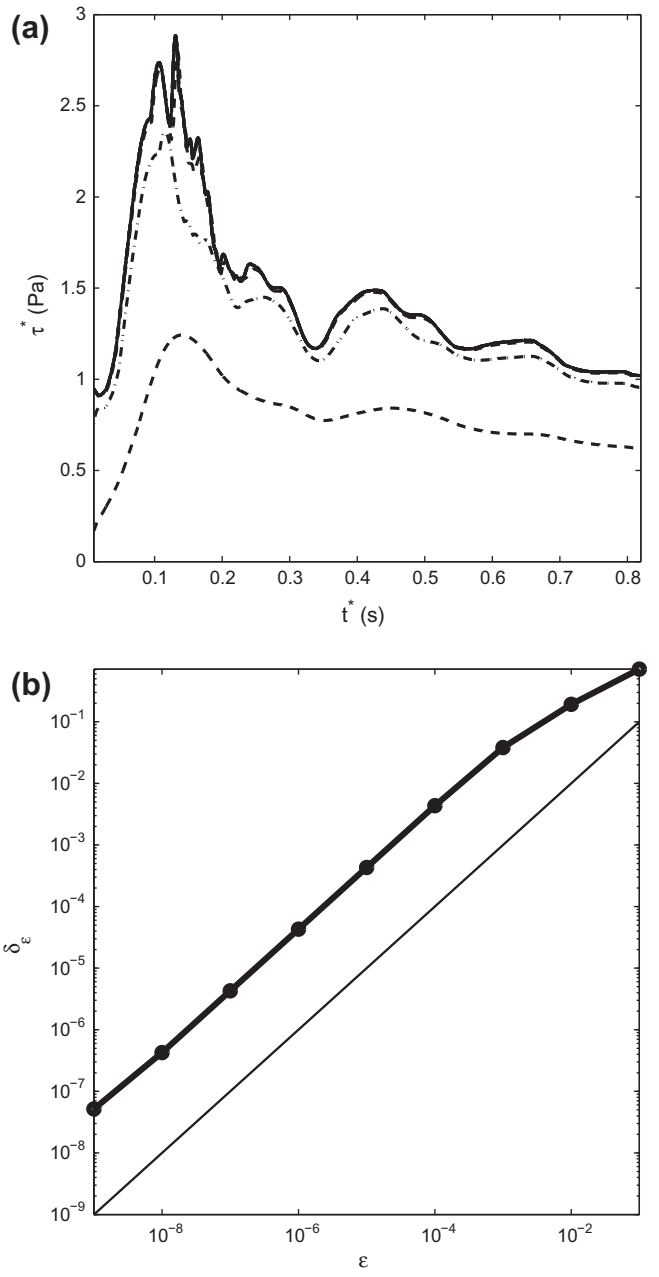

Fig. 8. Simulation of pulsatile flow at $Re = 250$ for the reference geometry at a range of the penalty parameter ε. Maximum shear stress responses for one typical pulse of duration 0.82 s (a) for different ε (dash, dash-dot) parameters show convergence to the solid line, which corresponds to the numerical solution computed with $\varepsilon = 10^{-10}$. In (b) we illustrate the L_2 norm of the difference between the maximum shear stress responses obtained at $\varepsilon = 10^{-1}, 10^{-2}, \ldots 10^{-9}$ and the solution computed at the smallest $\varepsilon = 10^{-10}$.

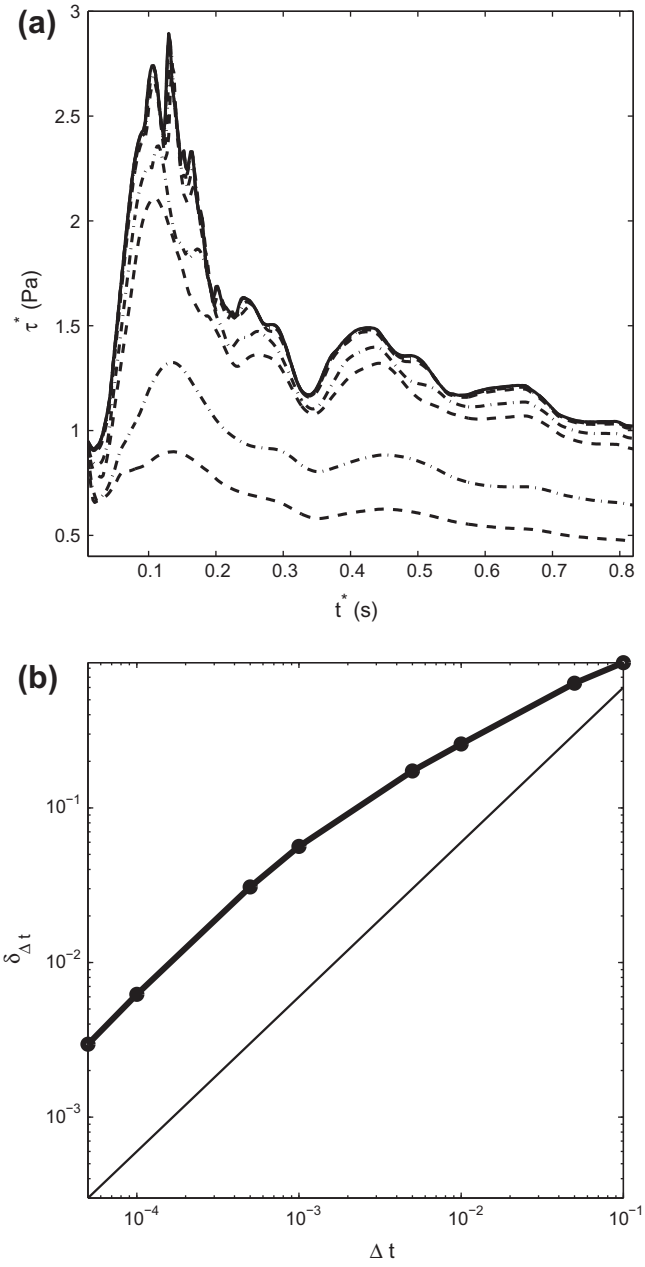

Fig. 9. Simulation of pulsatile flow at $Re = 250$ for the reference geometry computed with different time steps $\Delta t = 10^{-1}, \ldots, 10^{-5}$. Maximum shear stress response for one pulse of duration 0.82 s (a) for different Δt (alternating dash and dash-dot) show clear convergence to the solid line, which corresponds to the numerical solution computed at $\Delta t = 10^{-5}$. In (b) we illustrate the L_2 norm of the difference between the maximum shear stress response obtained at every $\Delta t = 10^{-1}, 5 \times 10^{-2}, 10^{-2}, 5 \times 10^{-3}, 10^{-3}, \ldots, 10^{-5}$ and the solution computed at the smallest time step $\Delta t = 10^{-5}$. Simulations are done at a grid resolution of $64 \times 32 \times 64$.

4. Transitional pulsatile flow

In this Section we first show the occurrence of transition in pulsatile flow in case the Reynolds number increases from the normal range around $Re = 250$ to the pathological range as high as $Re = 400$ (Section 4.1). Then we establish the robustness of this phenomenon by showing that it can be observed in a variety of flow properties and that it arises at basically all locations in the domain (Section 4.2). This motivates to have a closer look at the transition by considering the full dynamic spectrum of pressure and velocity response (Section 4.3).

4.1. Shear stress response in normal and pathological flow

Experimental observations of 'turbulence' inside cerebral aneurysms were presented in [9], confirmed by clinical study where high frequency 'bruits' were measured by a phonocatheter. Later, in [19,20] alternative clinical studies were presented, where in a non-invasive way intracranial blood flow sounds were recorded and analyzed. It was shown that certain high frequency sounds are present in patients with cerebrovascular diseases and not in healthy people. This suggests that if a cerebral aneurysm is present, qualitative changes in the flow may occur which lead to high-frequency bruits.

Is it possible to hear an aneurysm? Can one hear one's own aneurysm? Can critical aneurysms be detected by analyzing sound? Motivated by the experimental observations and these questions, we decided to perform a set of simulations at different Reynolds numbers. We consider the reference flow at $Re = 250$ to correspond to healthy cerebral blood flow circulation. Next to this we also perform simulations at pathological flow conditions:

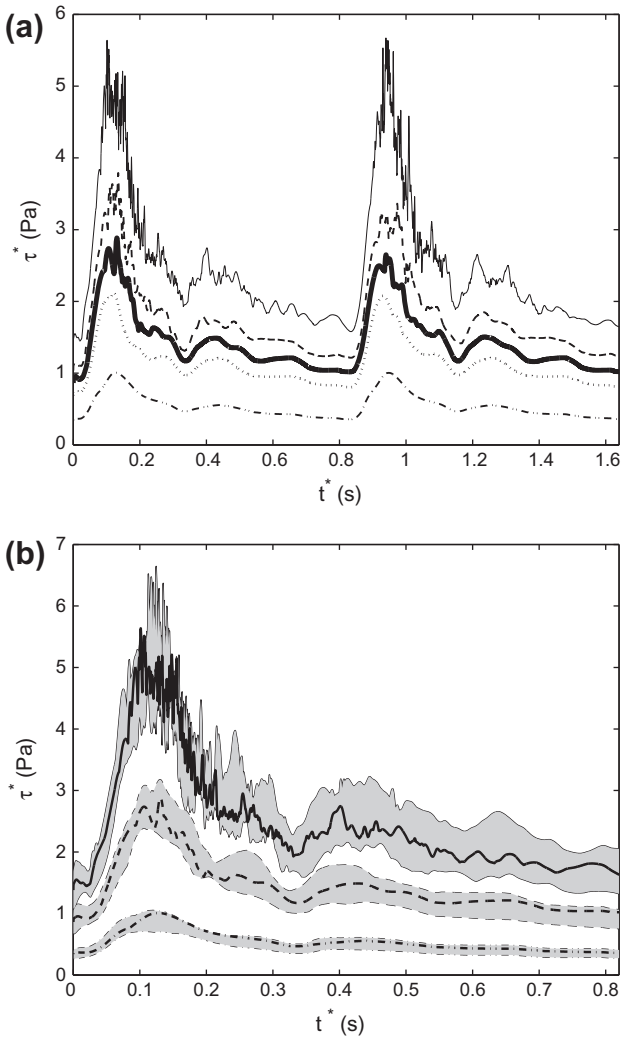

Fig. 10. Maximal shear stress for realistic pulsatile flow in the aneurysm geometry (a) and bounding solutions representing sensitivity to small differences in the geometry (b). In (a) the results for the reference flow at $Re = 250$ are shown in bold solid. Lower values for the Reynolds number are shown as $Re = 200$ (dot), $Re = 100$ (dash-dot), while higher values are displayed as $Re = 300$ (dash) and $Re = 400$ (thin, solid). In (b) the solid line is used for results at $Re = 400$, dash for $Re = 250$ and dash-dot for $Re = 100$. Gray bands represent how inner and outer solutions bound the basic solution at all Reynolds numbers.

at lower Reynolds numbers $Re = 100, 200$ and at higher Reynolds numbers $Re = 300, 400$. The range $Re = 100$–400 was motivated in Section 3.1 as a physiologically realistic regime for cerebral blood flow.

We compute pulsatile flow at different Reynolds numbers for a time corresponding to 10 pulses. In Fig. 10(a) we present the dynamic response of the maximum shear stress only for 2 pulse cycles in order to appreciate in more detail different levels of magnitude and dynamical patterns at different Reynolds numbers. The mean value averaged over 10 pulses at $Re = 250$ is found to be around 1.4 Pa with peak values near 2.6 Pa. At higher (possibly pathological) Reynolds number $Re = 400$ we observe a change in mean value up to 2.5 Pa and a considerable increase in peak values to 6.2 Pa averaged over 10 pulses. These values show the same general magnitude as reported in [13,32]. Transitional dynamics is clearly observed. Slow viscous flows at $Re = 100$ and $Re = 200$ smoothly follow the pulsatile forcing profile. At $Re = 250$ more dynamics appears to happen especially during the systole decay phase. The most interesting flows are at $Re = 300$ and $Re = 400$, where the nonlinear consequences of Navier–Stokes dynamics are firmly present. This transition was also observed in simulations of other realistic aneurysms and even for the simplified model aneurysms consisting of a curved vessel to which a spherical cavity was added [25].

In order to establish reliability of the transition we also recorded the response in nearby inner and outer bounding geometries, which was found to give practical bounding solutions [26,28]. These bounding geometries are based on the slight variations in the masking functions, which can be systematically generated while coarsening the grid for the initial medical data. Thus, for the geometry used in the current case-study, we started with $256 \times 256 \times 256$ grid, in which the geometry was obtained by direct transforming of the gray-scale voxels into the solid and fluid 3D-cells. While simplifying the geometry, we noticed that the main vessel was located only in the half of the original 'cube' of data, which allowed us to work with the $256 \times 128 \times 256$ grid as the finest one. During coarsening the grid, certain choices need to be done in order to determine whether the 3D-cell of the coarse grid is solid or fluid, depending on the property of the few cells of the finest mesh. At this stage 8 bounding geometries can be defined, next to the one basic geometry. More details about this procedure applied to the geometry used in this case-study and analysis of

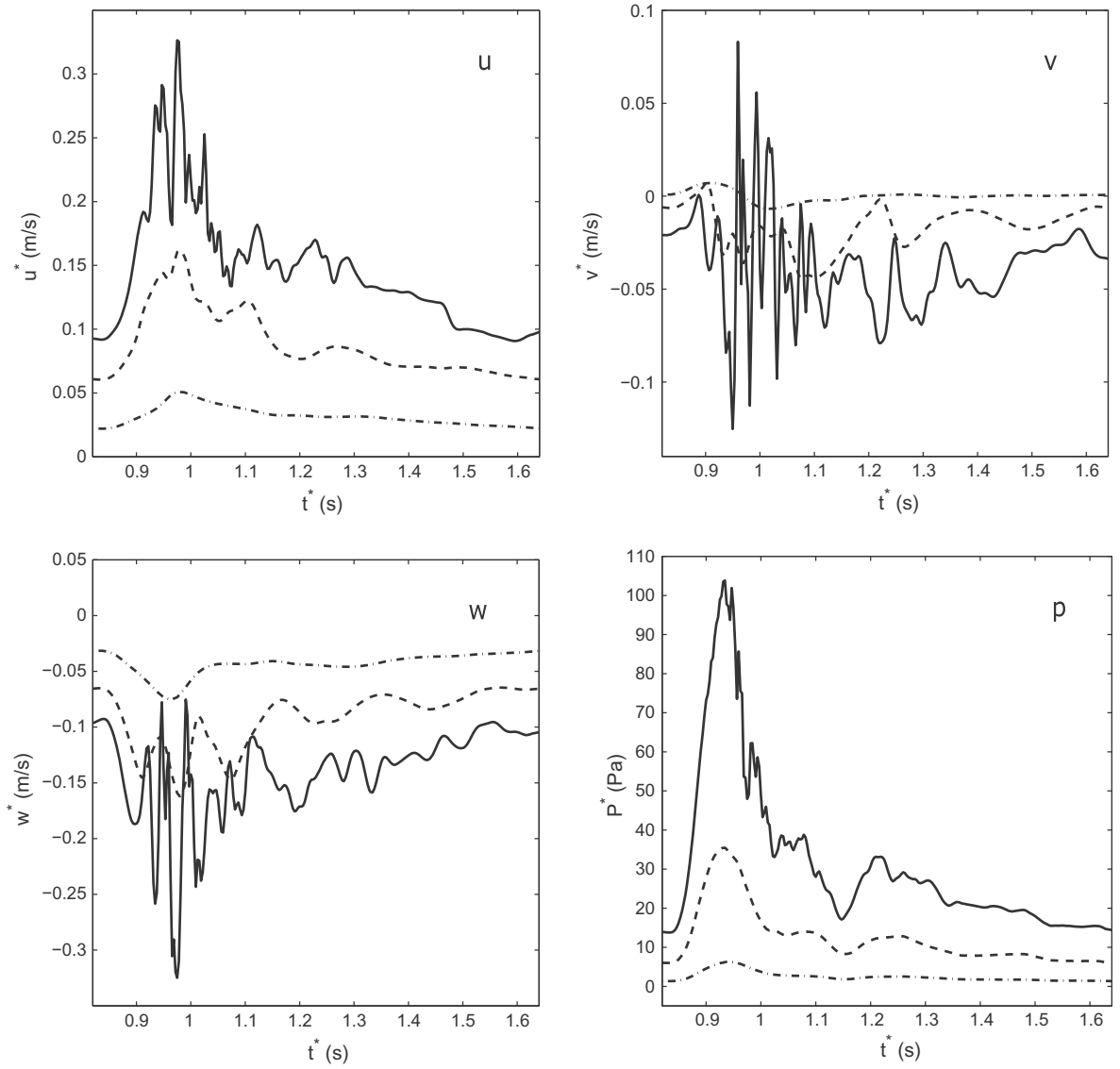

Fig. 11. Velocity components u, v, w and p at point 11 in the vessel opposite the aneurysm bulge. Transition at different Reynolds numbers is present for all these quantities. Simulations are at $Re = 100$ (dash-dot), $Re = 250$ (dash) and $Re = 400$ (solid).

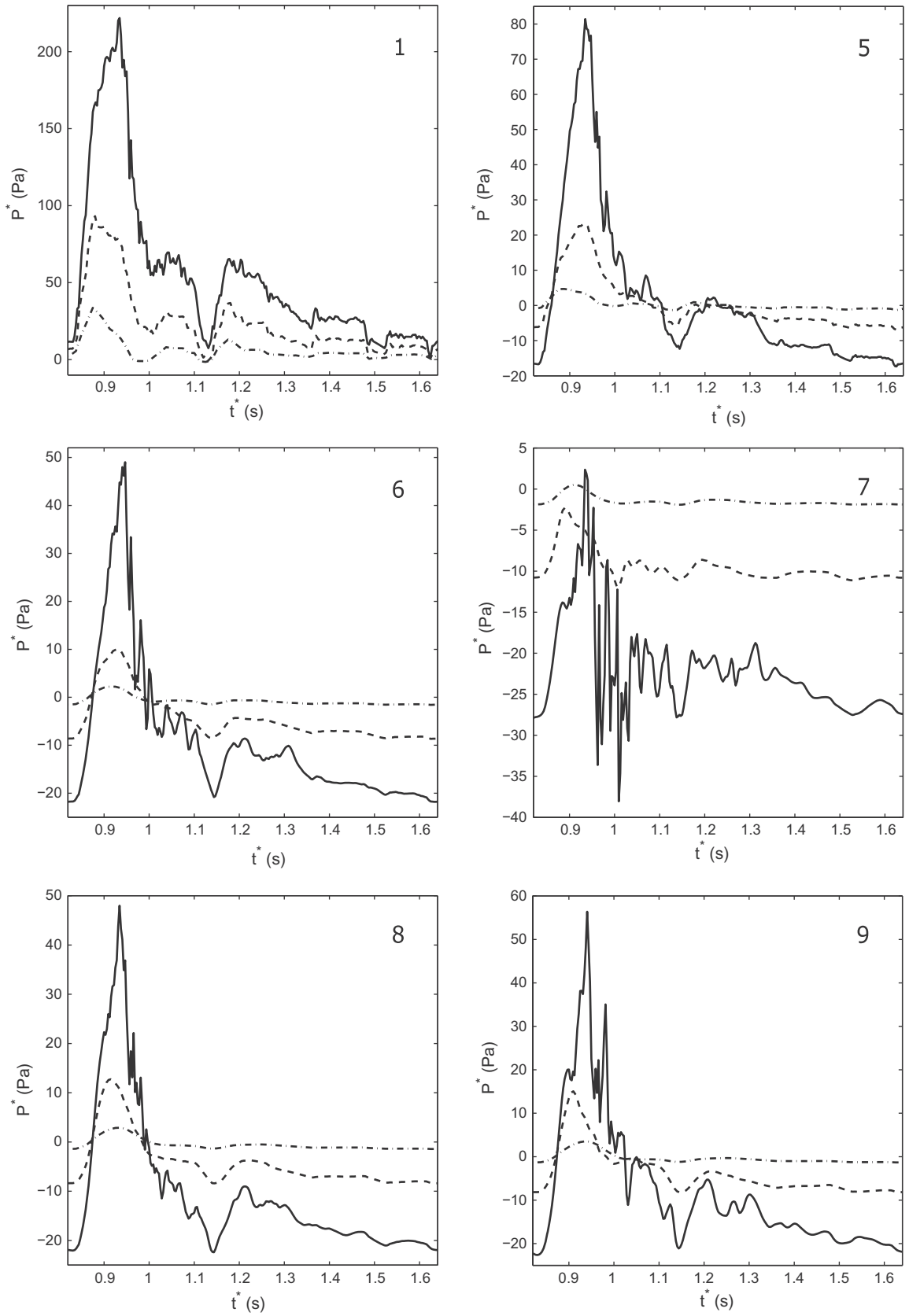

Fig. 12. Pressure relative to the time-averaged pressure at point 11 in 10 selected points inside the vessel and aneurysm as introduced in Fig. 1(b). The number on the top right of every sub-figure corresponds to the label of the point. Transition at different Reynolds numbers is present for all locations. Simulations are at $Re = 100$ (dash-dot), $Re = 250$ (dash) and $Re = 400$ (solid).

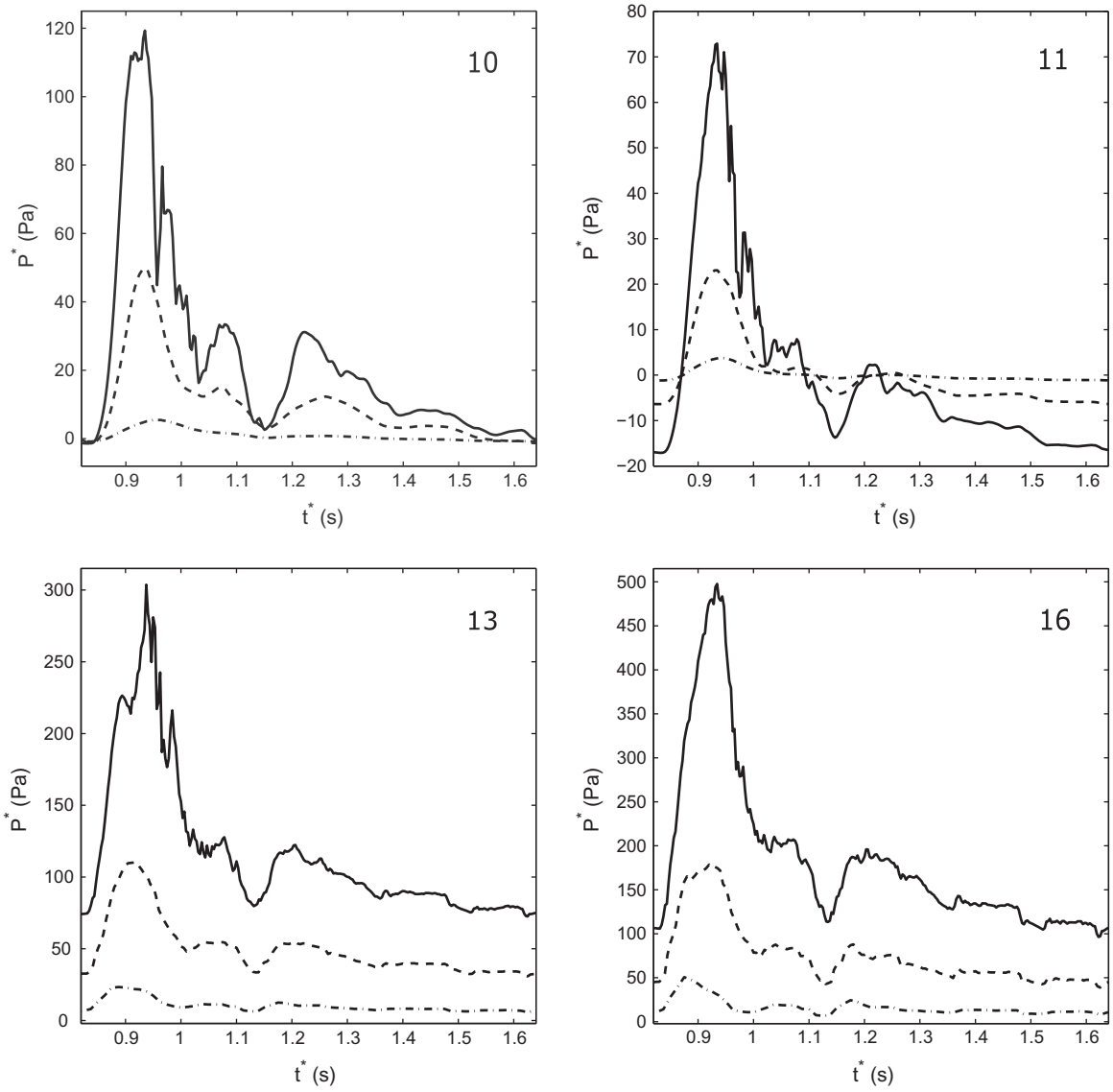

Fig. 12 (*continued*)

the 'fluid-volume' of obtained geometries can be found in [29]. Practical application of bounding geometries is in the solutions, which appear to be also bounded. This allows to predict the flow and a range of possible variations caused by the slight changes in the aneurysm geometry.

For pulsatile simulations we consider only nearby 'inner' and 'outer' geometries which have a slightly smaller and slightly larger volume of flow domain. These bounding geometries allow a narrow band of solutions, characterizing the sensitivity of the simulation results. In Fig. 10(b) we show the maximum shear stress during one cycle at three Reynolds numbers – in each case we collect the basic solution together with its two bounding solutions. The variability bands are plotted as gray shading allowing to appreciate better the dynamics of the bounding solutions. Thus, at $Re = 100$ and $Re = 250$ bounding solutions closely follow the basic solution, representing relatively narrow sensitivity bands with a general variability range of 10–15%. At $Re = 400$ the transition is present also in bounding solutions, leading to the wider variability band, with more increased peak values for the inner geometry. Now that we have transition established, we will consider the robustness of this phenomenon regarding flow-quantity and physical location at which transition is measured.

4.2. Robustness of pulsatile transition

In this subsection we will establish the robustness of the transition phenomena observed in the previous subsection. In particular, we will show that this phenomenon is equally present in a variety of flow properties such as the three velocity components and the pressure. This shows transition to be independent of the quantity that is being monitored. Subsequently, we will turn attention to the pressure response and show that the qualitative features of the transition appear similarly at different measuring points in the flow domain. This shows an independence of location.

In Fig. 11 we show the velocity components u, v and w and pressure p at point 11 (see Fig. 1(b)) during one pulse at three Reynolds numbers. We choose point 11 as the reference point due to its location - directly opposite of the aneurysm bulge. We observe the transition in all presented quantities. Not only levels for u, v, w and p are varying but also the dynamic pattern of the response during one cardiac cycle is changing considerably as a result of the transition. This illustrates the general independence of transition on observed flow-quantity.

In Fig. 12 we collect the pressure response during a pulsatile cycle in 8 characteristic measuring points selected form those

indicated in Fig. 1(b). We take the average pressure at point 11 as reference pressure and compare pressure response relative to this point. We observe that, although the precise pressure signal is different at each location, the general characteristic of smooth time-dependence at $Re = 100$ and 250 changes considerably at $Re = 400$.

4.3. Frequencies of the pulsatile solution

There are a few ways to measure the flow inside cerebral vessels and aneurysms: invasively, measuring pressure directly by inserting a pressure sensor on a catheter and non-invasively as, e.g., using TCD to obtain time-dependent mean velocity time traces in the arteries nearby the scalp. Sounds inside cerebral vessels can also be measured in both ways: with a phono-catheter [9] and with a sonic detector [19] or a transducer [20] which are applied close to the head or even attached to the scalp. Afterwards the signals recorded by any of the above listed techniques can be analyzed by considering their spectra.

We translated the numerical signals computed during one cycle into the corresponding spectra. As was shown in the previous subsection, transition occurs quite independently of flow-quantity and location at which it was measured. We concentrate on pressure and streamwise velocity component u as these would correspond roughly with the quantities that can be measured clinically. We analyze the spectra in four chosen points along the aneurysm geometry. In particular, we chose one point at the beginning of the aneurysm geometry (point 1), where flow is close to a Poiseuille type flow. We also include point 11, located opposite the aneurysm bulge. Two more points are 7 and 10, which are inside the aneurysm bulge at different distances from the main vessel (see Fig. 1(b)). Similar choices for points of interest near and inside the aneurysm are shown in [1,9].

In Fig. 13 we show the Fourier transform of the pressure computed at three flow regimes in four chosen points. The actual frequencies are represented on the horizontal axis. The main component due to the cardiac cycle of 0.82 s is clearly observed at 1.22 Hz. On the vertical axis we plot the square of the coefficients of the Fourier transform of the time-trace of the pressure. We plot all the spectra on the same scale to facilitate comparison of the values. Transition in the flow due to different Reynolds numbers is shown in terms of much higher values for the high frequencies. In point 1 all the signals seem to give similar spectra. This suggests that in a roughly cylindrical vessel the flow keeps its properties at $Re = 100, 250$ and 400. In the other points we see

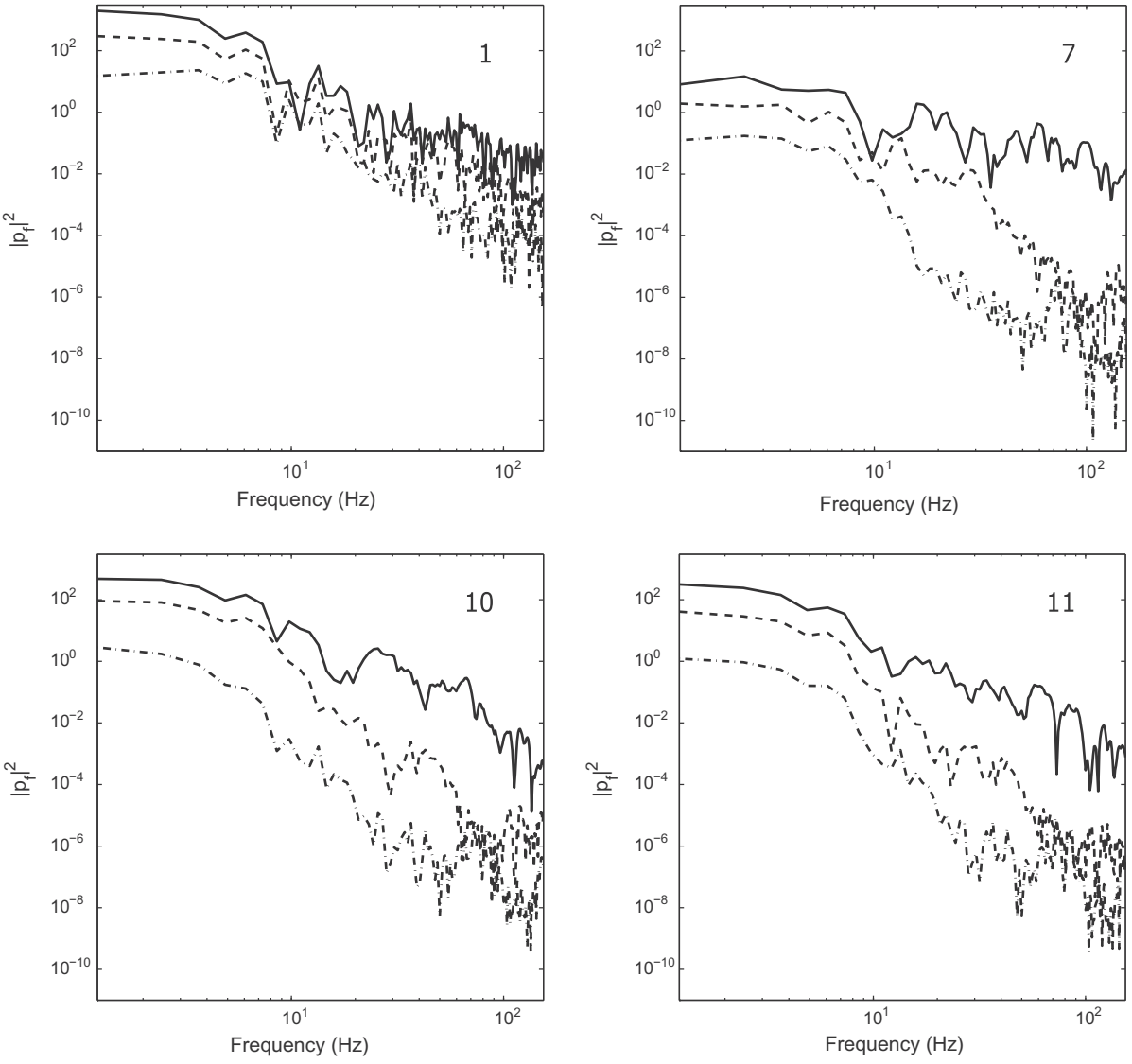

Fig. 13. Fourier transform of the pressure signals at three different Reynolds numbers in 4 points in the vessel in the beginning of the flow domain (point 1), close to the aneurysm bulge (point 11) and inside the aneurysm bulge (points 7, 10). Simulations are at $Re = 100$ (dash-dot), $Re = 250$ (dash) and $Re = 400$ (solid).

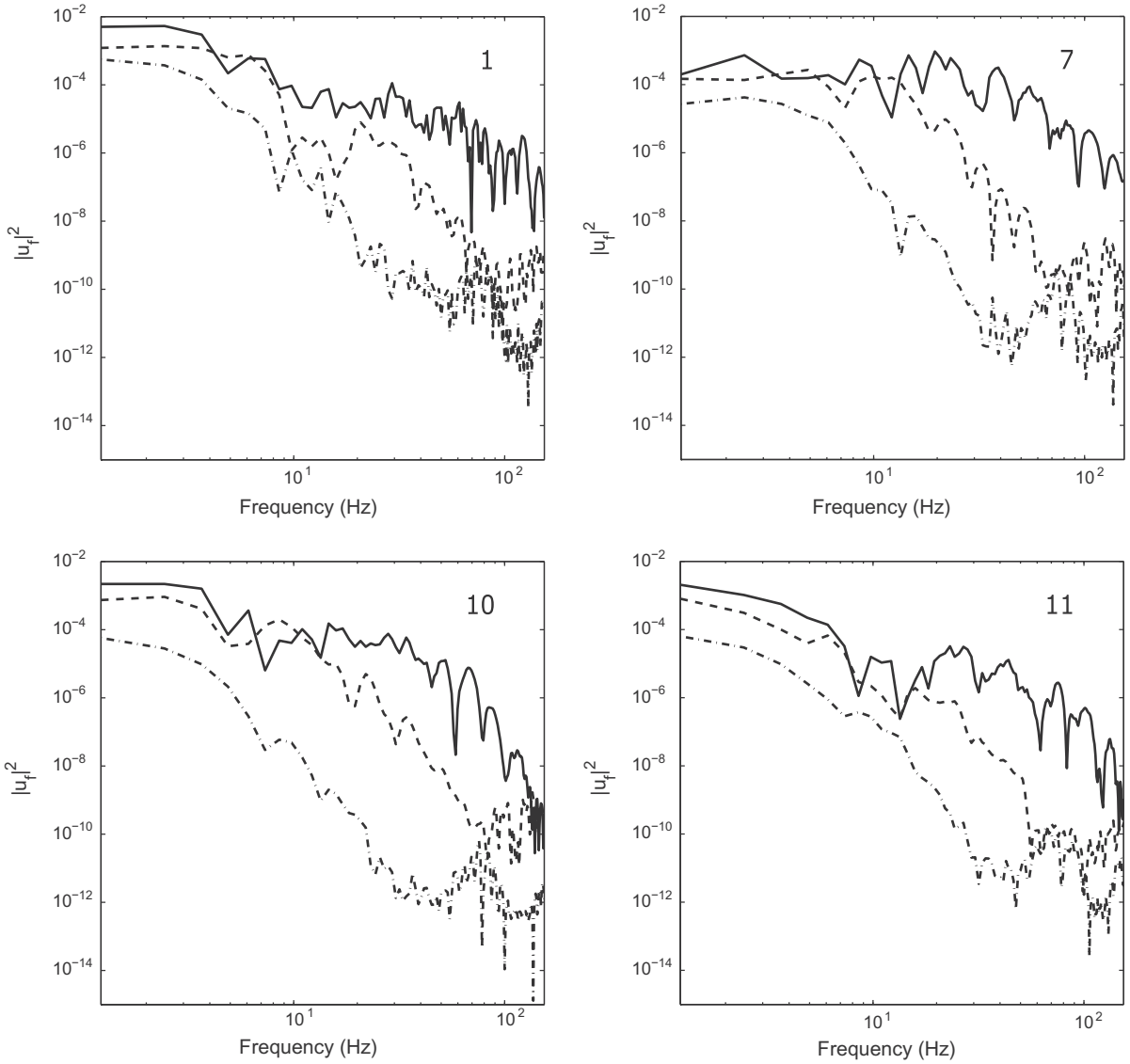

Fig. 14. Fourier transform of the velocity signals at three different Reynolds numbers in 4 points in the vessel in the beginning of the flow domain (point 1), close to the aneurysm bulge (point 11) and inside the aneurysm bulge (points 7, 10). Simulations are at $Re = 100$ (dash-dot), $Re = 250$ (dash) and $Re = 400$ (solid).

more dynamics in the small scales. We also notice that the difference between the tails of the spectra when comparing different Reynolds numbers increases. Even though the spectra have quite wiggly tails, the general levels of high frequency components can be readily identified.

In Fig. 14 the Fourier transform of the u velocity component is shown in the same four points. On the vertical axis we plot the square of the coefficients of the Fourier transform of the u velocity time trace. The flow patterns again display transition with increasing Reynolds number. In all points the spectrum at $Re = 400$ is well separated from the other recordings, showing the increased presence of components of high frequencies. Interestingly, the tail of the velocity spectra for the velocities is rather smooth for the lower Reynolds numbers.

5. Concluding remarks

In this paper we presented a complete computational model for the simulation of pulsatile blood flow in cerebral aneurysms. Based on the volume penalizing IB method, the current model allows to compute flow and forces that emerge in aneurysms under pulsatile flow conditions. We analyzed several solutions at different flow regimes and observed strong transition to complex time-dependence at higher Reynolds number, which may be of interest for medical monitoring. We emphasized this point in terms of presenting time-traces of the solution as well as the corresponding spectra.

The aneurysm geometry considered in this study was reconstructed from 3DRA medical data. The IB method allows a quite direct transformation of the gray scale voxels contained in the images into fluid and solid 3D cells in the computational domain. Flow conditions corresponding to physiologically relevant cerebral flows were estimated, based on data obtained from literature. Numerous clinical studies show variability of the measured sizes of cerebral arteries, ranges for blood flow velocity and viscosity. Combining the variability ranges of these components we arrived at the approximate range of flow conditions, that would apply for cerebral flow in the Circle of Willis. As a typical reference cerebral flow we considered $Re = 250$. When taking into account all the uncertainties we obtained flows in a range of $100 \leqslant Re \leqslant 400$. At these different flow conditions we performed pulsatile flow

simulations. The main purpose of this study was not just to compute the flow with given parameters, but to assess how the variability in the parameters translates into a confidence interval around the basic final solution.

For the reference flow we illustrated the influence of partial filling of the aneurysm bulge on the flow pattern that develops inside. This type of simulations can support coiling procedures in taking a decision about the amount of coil that is required to change the flow sufficiently to remove the problem for the patient.

The imposed pulsatile profile was obtained from TCD measurements of the velocity of the blood flow in the middle cerebral artery in the brain. We chose a typical pulse, normalized it and translated this into the volumetric flow rate assuming a circular cross-section of the vessel. We repeated this signal periodically as flow forcing which leads to a model for the time-dependent pulsatile flow. We performed pulsatile simulations at different Reynolds numbers and analyzed the main solution and its components. In particular, we considered velocity, pressure and maximum shear stress.

Increasing or decreasing the Reynolds number has a marked effect on the dynamic response. At the lower Reynolds numbers the response of the solution is seen to be smooth, following the imposed pulsatile profile. At the higher Reynolds numbers the natural Navier–Stokes nonlinearity seems to become dominant, which makes the numerical response lively by the emergence of relatively high frequency components of the solution. In addition, the amplitude of the solution components rises considerably, clearly expressing the transition towards complex pulsatile flow in which much higher frequencies gain in dynamic importance. We investigated in more detail this transition and showed that it is robust to choice of the computed quantity and to the location in the aneurysm geometry. The method of bounding solutions was employed to arrive at a confidence interval around the basic solution - this was illustrated for the time-dependent maximum shear stress. Furthermore, we looked into the spectra for the pressure and streamwise velocity. Much higher levels of both - high and low frequencies arise at increased Reynolds number, which may be associated with an increased risks to the patient. Recording the spectrum of frequencies and analyzing trends in their levels may become relevant in medical practice and used as an easy monitoring procedure.

Acknowledgements

The authors gratefully acknowledge NCF support through Project SH061, for computations at the Huygens computer at SARA (Amsterdam, The Netherlands). This study was made possible through funding from the University of Twente alone.

References

[1] Baek H, Jayaraman MV, Richardson PD, Karniadakis GE. Flow instability and wall shear stress variation in intracranial aneurysms. J R Soc Interface 2009;7:967–88. http://dx.doi.org/10.1098/rsif.2009.0476.
[2] Batchelor GK. An introduction to fluid dynamics. Cambridge University Press; 2007.
[3] Bernsdorf J, Wang D. Non-Newtonian blood flow simulation in cerebral aneurysms. Comp Math Appl 2009;58:1024–9.
[4] Boussel L, Rayz V, McCulloch C, Martin A, Acevedo-Bolton G, Lawton M, et al. Aneurysm growth occurs at region of low wall shear stress: patient-specific correlation of hemodynamics and growth in a longitudinal study. Stroke 2008;39:2997–3002.
[5] Cebral JR, Castro MA, Burgess JE, Pergolizzi RS, Sheridan MJ, Putman CM. Characterization of cerebral aneurysms for assessing risk of rupture by using patient-specific computational hemodynamics models. AJNR Am J Neuroradiol 2005;26:2550–9.
[6] Cebral JR, Castro MA, Appanaboyina S, Putman CM, Millan D, Frangi AF. Efficient pipeline for image-based patient-specific analysis of cerebral aneurysms hemodynamics: technique and sensitivity. IEEE Trans Med Imaging 2005;24:457–67. http://dx.doi.org/10.1109/TMI.2005.844159.
[7] Cebral JR, Mut F, Weir J, Putman C. Quantitative characterization of the hemodynamic environment in ruptured and unruptured brain aneurysms. AJNR Am J Neuroradiol 2011;32:145–51. http://dx.doi.org/10.3174/ajnr.A2419.
[8] Duijvenboden S, Schaafsma A, Geurts BJ. Usefulness of schrodingerś operator for assessing new parameters in Transcranial Doppler sonography. University of Twente, Internal Report; 2011.
[9] Ferguson GG. Turbulence in human intracranial saccular aneurysms. J Neurosurg 1970;33:485–97.
[10] Gambaruto AM, Janela J, Moura A, Sequeira A. Sensitivity of hemodynamics in a patient specific cerebral aneurysm to vascular geometry and blood rheology. Math Biosci Eng 2011;8:409–23. http://dx.doi.org/10.3934/mbe.2011.8.409.
[11] Geurts BJ. Elements of direct and large-eddy simulation. Edwards Publishing; 2003. ISBN: 1-930217-07-2.
[12] Gijsen FJH, van de Vosse FN, Janssen JD. The influence of the non-Newtonian properties of blood on the flow in large arteries: steady flow in a carotid bifurcation model. J Biomech 1999;32:601–8.
[13] Goubergrits L, Schaller J, Kertzscher U, van der Bruck N, Poethkow K, Petz Ch, et al. Statistical wall shear stress maps of ruptured and unruptured middle cerebral artery aneurysms. J R Soc Interface 2012;9:677–88. http://dx.doi.org/10.1098/rsif.2011.0490.
[14] Hendrikse J, van Raamt AF, van der Graaf Y, Mali WPTM, van der Grond J. Distribution of cerebral blood flow in the circle of willis. Radiol 2005;235:184–9. http://dx.doi.org/10.1148/radiol.2351031799.
[15] Hollnagel DI, Summers PE, Poulikakos D, Kollias SS. Comparative velocity investigations in cerebral arteries and aneurysms: 3D phase-contrast MR angiography, laser Doppler velocimetry and computational fluid dynamics. NMR Biomed 2009;22:795–808. http://dx.doi.org/10.1002/nbm.1389.
[16] Janela J, Moura A, Sequeira A. A 3D non-Newtonian fluid-structure interaction model for blood flow in arteries. J Comp Appl Math 2010;234:2783–91. http://dx.doi.org/10.1016/j.cam.2010.01.032.
[17] Kamath S. Observations on the length and diameter of vessels forming the Circle of Willis. J Anatomy 1981;133:419–23.
[18] Ku DN. Blood flow in arteries. An Rev Fluid Mech 1997;29:399–434.
[19] Kosugi Y, Goto T, Ikebe J, Joshita H, Takakura K. Sonic detection of intracranial aneurysm and AVM. Stroke 1983;14:37–42.
[20] Kurokawa Y, Abiko S, Watanabe K. Noninvasive detection of intracranial vascular lesions by recording blood flow sounds. Stroke 1994;25:397–402. http://dx.doi.org/10.1161/01.STR.25.2.397.
[21] Lopez Penha DJ, Geurts BJ, Stolz S, Nordlund M. Computing the apparent permeability of an array of staggered square rods using volume-penalization. Comput Fluids 2011;51:157–73. http://dx.doi.org/10.1016/j.compfluid.2011.08.011.
[22] Mantha AR, Benndorf G, Hernandez A, Metcalfe RW. Stability of pulsatile blood flow at the ostium of cerebral aneurysms. J Biomech 2009;42:1081–7.
[23] Metcalfe RW. The promise of computational fluid dynamics as a tool for delineating therapeutic options in the treatment of aneurysms. AJNR Am J Neuroradiol Editorials 2003;24:553–4.
[24] Mikhal J, Lopez Penha DJ, Stolz S, Geurts BJ. Application of an immersed boundary method to flow in cerebral aneurysms and porous media, In: Proceedings of FEDSM, ASME 2010, Am Soc Mech Eng, 31042; 2010.
[25] Mikhal J, Geurts BJ. Pulsatile flow in model cerebral aneurysms. Proc Comput Sci 2011;4:811–20. http://dx.doi.org/10.1016/j.procs.2011.04.086.
[26] Mikhal J, Geurts BJ. Bounding solutions for cerebral aneurysms. New Archive Math 2011;5:163–8.
[27] Mikhal J, Slump CH, Geurts BJ. Simulation of pulsatile flow in cerebral aneurysms: from medical images to flow and forces. In: Murai Y, editor. Aneurysm. InTech; 2012. doi:10.5772/47858, ISBN: 978-953-51-0730-9.
[28] Mikhal J, Geurts BJ. Development and application of a volume penalization immersed boundary method for the computation of blood flow and shear stresses in cerebral vessels and aneurysms. J Math Biol 2013;67:1847–75. http://dx.doi.org/10.1007/s00285-012-0627-5. Published online November 2012.
[29] Mikhal J, Kroon DJ, Slump CH, Geurts BJ. Flow prediction in cerebral aneurysms based on geometry reconstruction from 3D rotational angiography. Int J Num Meth Biomed Eng 2013;29:777–805. http://dx.doi.org/10.1002/cnm.2558.
[30] Mittal R, Iaccarino G. Immersed boundary methods. An Rev Fluid Mech 2005;37:239–61. http://dx.doi.org/10.1146/annurev.fluid.37.061903.175743.
[31] Oktar SO, Yücel C, Karaosmanoglu D, Akkan K, Ozdemir H, Tokgoz N, et al. Blood-flow volume quantification in internal carotid and vertebral arteries: comparison of 3 different ultrasound techniques with phase-contrast MR imaging. AJNR Am J Neuroradiol 2006;27:363–9.
[32] Oyre S, Ringgaard S, Kozerke S, Paaske WP, Erlandsen M, Boesiger P, et al. Accurate noninvasive quantification of blood flow, cross-sectional lumen vessel area and wall shear stress by three-dimensional paraboloid modeling of magnetic resonance imaging velocity data. J Am College Cardiol 1998;32:128–34.
[33] Passerini T, de Luca M, Formaggia L, Quarteroni A, Veneziani A. A 3D/1D geometrical multiscale model of cerebral vasculature. J Eng Math 2009;64:319–30. http://dx.doi.org/10.1007/s10665-009-9281-3.
[34] Passerini T, Sangalli LM, Vantini S, Piccinelli M, Bacigaluppi S, Antiga L, et al. An integrated statistical investigation of internal carotid arteries of patients affected by cerebral aneurysms. Cardiovasc Eng Tech 2012;1:26–40. http://dx.doi.org/10.1007/s13239-011-0079-x.
[35] Perktold K, Peter R, Resch M. Pulsatile non-Newtonian blood flow simulation through a bifurcation with an aneurysm. Biorheol 1989;26:1011–30.

[36] Quarteroni A, Formaggia L. Mathematical modelling and numerical simulation of the cardiovascular system. Handbook of numerical analysis. Amsterdam: North-Holland; 2004.
[37] Ringelstein EB, Kahlscheuer B, Niggemeyer E, Otis SM. Transcranial doppler sonography: anatomical landmarks and normal velocity values. Ultrasound Med Biol 1990;16:745–61.
[38] Sforza DM, Löhner R, Putman C, Cebral J. Hemodynamic analysis of intracranial aneurysms with moving parent arteries: basilar tip aneurysms. Int J Num Meth Biomed Eng 2010;26:1219–27. http://dx.doi.org/10.1002/cnm.1385.
[39] Spalart PR. Direct simulation of a turbulent boundary layer up to Rtheta = 1410. J Fluid Mech 1988;187:61–98. http://dx.doi.org/10.1017/S0022112088000345.
[40] Steinman DA, Milner JS, Norley CJ, Lownie SP, Holdsworth DW. Image-based computational simulation of flow dynamics in a giant intracranial aneurysm. AJNR Am J Neuroradiol 2003;24:559–66.
[41] Turowski B, Macht S, Kulcsár Z, Hänggi D, Stummer W. Early fatal hemorrhage after endovascular cerebral aneurysm treatment with a flow diverter (SILK-Stent): do we need to rethink our concepts? Neuroradiology 2011;53:37–41. http://dx.doi.org/10.1007/s00234-010-0676-7.
[42] van Ooij P, Guédon A, Poelma C, Schneiders J, Rutten MCM, Marquering HA, et al. Complex flow patterns in a real size intracranial aneurysm phantom: phase contrast MRI compared with particle image velocimetry and computational fluid dynamics. NMR Biomed 2012;25:14–26. http://dx.doi.org/10.1002/nbm.1706.
[43] van Rooij WJ, Sprengers ME, de Gast AN, Peluso APP, Sluzewski M. 3D rotational angiography: the new gold standard in the detection of additional intracranial aneurysms. AJNR Am J Neuroradiol 2008;29:976–9. http://dx.doi.org/10.3174/ajnr.A0964.
[44] Venugopal P, Valentino D, Schmitt H, Villablanca JP, Viñuela F, Duckwiler G. Sensitivity of patient-specific numerical simulation of cerebral aneurysm hemodynamics to inflow boundary conditions. J Neurosurg 2007;106:1051–60.
[45] Verstappen RWCP, Veldman AEP. Symmetry-preserving discretization of turbulent flow. J Comp Phys 2003;187:343–68.
[46] Wanke I, Dörfler A, Forsting M. Intracranial aneurysms. Intracranial vascular malformations and aneurysms. Springer; 2008. ISBN: 978-3-540-32919-0.